Cell Reports

Article

# Spatial regulation of coordinated excitatory and inhibitory synaptic plasticity at dendritic synapses

## Graphical abstract

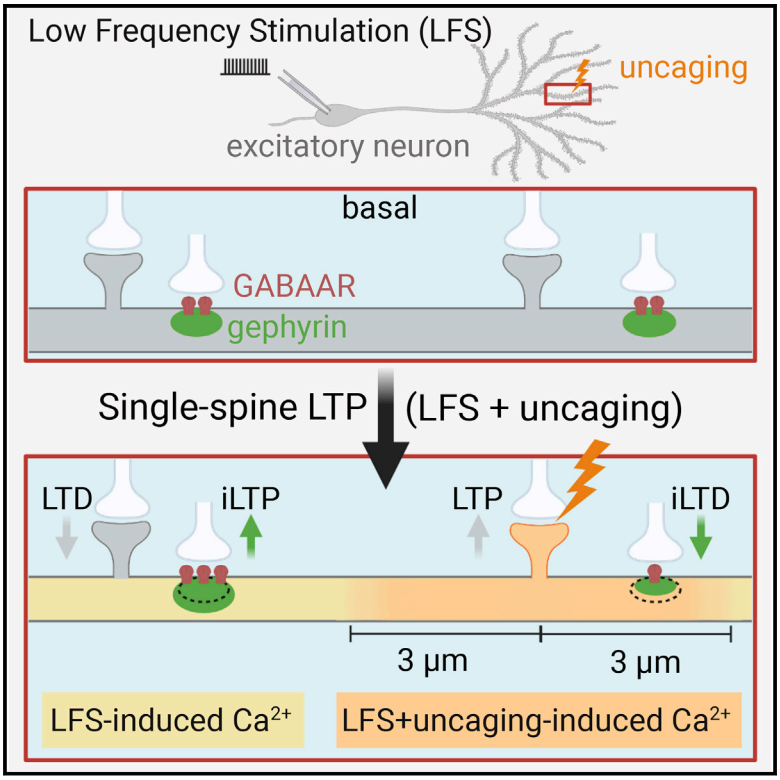


## Highlights

- LTP of individual dendritic spines causes iLTD at neighboring GABAergic synapses
- Interaction between single-spine LTP and iLTD occurs in the spatial range of ±3 µm
- This iLTD depends on the local dendritic calcium increase and calpain activation
- iLTD is associated with reduced gephyrin clustering and increased GABAAR mobility


## Authors

Tiziana Ravasenga, Massimo Ruben, Vincenzo Regio, Alice Polenghi, Enrica Maria Petrini, Andrea Barberis

## Correspondence

andrea.barberis@iit.it



## In brief

How do neighboring dendritic excitatory and inhibitory synapses interact in hippocampal neurons? Here, Ravasenga et al. reveal the spatial rules of heterosynaptic plasticity by demonstrating that LTP at an individual dendritic spine depresses adjacent GABAergic synapses in the range of ±3 µm.


Ravasenga et al., 2022, Cell Reports *38*, 110347
February 8, 2022 
https://doi.org/10.1016/j.celrep.2022.110347

CellPress

Cell Reports

CellPress
OPEN ACCESS

Article

# Spatial regulation of coordinated excitatory and inhibitory synaptic plasticity at dendritic synapses

Tiziana Ravasenga,[1,2] Massimo Ruben,[1,2] Vincenzo Regio,[1] Alice Polenghi,[1] Enrica Maria Petrini,[1] and Andrea Barberis[1,3,*]

[1]Neuroscience and Brain Technologies Department, Fondazione Istituto Italiano di Tecnologia, Via Morego 30, 16163 Genova, Italy
[2]These authors contributed equally
[3]Lead contact
*Correspondence: andrea.barberis@iit.it
https://doi.org/10.1016/j.celrep.2022.110347

## SUMMARY

The induction of synaptic plasticity at an individual dendritic glutamatergic spine can affect neighboring spines. This local modulation generates dendritic plasticity microdomains believed to expand the neuronal computational capacity. Here, we investigate whether local modulation of plasticity can also occur between glutamatergic synapses and adjacent GABAergic synapses. We find that the induction of long-term potentiation at an individual glutamatergic spine causes the depression of nearby GABAergic inhibitory synapses (within 3 μm), whereas more distant ones are potentiated. Notably, L-type calcium channels and calpain are required for this plasticity spreading. Overall, our data support a model whereby input-specific glutamatergic postsynaptic potentiation induces a spatially regulated rearrangement of inhibitory synaptic strength in the surrounding area through short-range heterosynaptic interactions. Such local coordination of excitatory and inhibitory synaptic plasticity is expected to influence dendritic information processing and integration.

## INTRODUCTION

Similarly to glutamatergic synapses, GABAergic synapses undergo many forms of short- and long-term plasticity expressed at both the pre- and postsynaptic levels (Castillo et al., 2011; Chiu et al., 2019; Barberis, 2019). This raises the important question of how excitatory and inhibitory synaptic plasticity are orchestrated during neuronal activity. Several studies show that the chronic modification of overall neuronal spiking activity can modulate both glutamatergic and GABAergic synapses within the same neuron, thus indicating the presence of cellular mechanisms coordinating activity-dependent changes in synaptic excitatory and inhibitory strength (Ibata et al., 2008; Rannals and Kapur, 2011; Turrigiano, 1999, 2011). However, the precise relationship between neuronal activity and the concomitant modifications of both glutamatergic and GABAergic synapses is poorly understood. This is mainly because the effects of diverse acute plasticity-inducing protocols have been mostly studied independently at either excitatory or inhibitory synapses.

Nevertheless, the induction and expression of glutamatergic and GABAergic plasticity show several common features. At postsynaptic level, the activation of NMDA receptors and CaMKII, one of the best characterized signaling pathways in excitatory glutamatergic long-term potentiation (LTP) (Nicoll and Roche, 2013), is also crucial for the expression of inhibitory long-term potentiation (iLTP) (Chiu et al., 2018; Flores et al., 2015; He et al., 2015; Kano et al., 1996; Marsden et al., 2007; Petrini et al., 2014). Moreover, GABAergic postsynaptic depression relies on the activity of calcineurin (Bannai et al., 2009, 2015; Muir et al., 2010), a phosphatase that is also implicated in glutamatergic LTD (Mulkey et al., 1994; Zeng et al., 2001). In addition the proteolytic action of calpains has been reported to affect both glutamatergic and GABAergic synaptic plasticity (Andres et al., 2013; Briz and Baudry, 2017; Costa et al., 2016; Tyagarajan et al., 2013). Along the same lines, postsynaptic glutamatergic and GABAergic plasticity involve the modulation of synaptic receptor number and lateral diffusion and their interaction with scaffold molecules (Bannai et al., 2009; Kurotani et al., 2008; Muir et al., 2010; Nusser et al., 1998; Petrini et al., 2014; Diering and Huganir, 2018; Carta et al., 2013; Choquet and Triller, 2013).

Importantly, inhibitory synapses, at least in specific dendritic sub-regions, can be located only few micrometers away from glutamatergic synapses (Megías et al., 2001; Iascone et al., 2020) or even impinge on spines (Nusser et al., 1996; Tamás et al., 2003; Villa et al., 2016). Thus, the analogous mechanisms of postsynaptic plasticity and the spatial contiguity of GABAergic and glutamatergic synapses suggest the hypothesis of local interplay in dendrites during synaptic plasticity between neighboring excitatory and inhibitory synapses.

In the present study, we investigated the spatial determinants involved in the interaction between hippocampal dendritic excitatory and inhibitory synapses. By exploiting different experimental approaches we show a high degree of coordination between plasticity at glutamatergic and GABAergic synapses

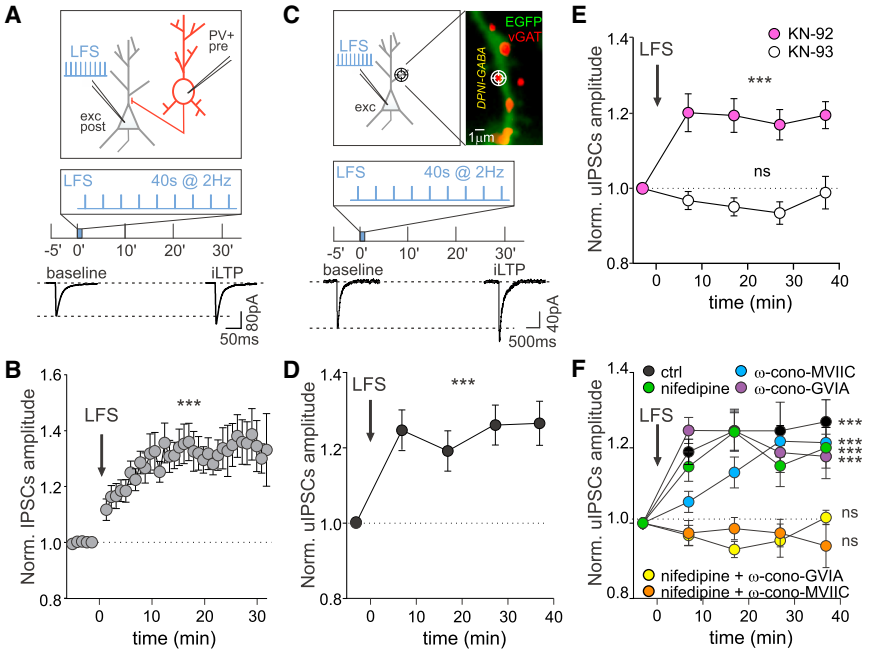


**Figure 1. LFS induces iLTP at GABAergic synapses**

(A) Top: Experimental configuration of paired-patch recordings including an electrically stimulated presynaptic parvalbumin-tdTomato positive (PV+) interneuron (red) and a postsynaptic excitatory hippocampal neuron (gray) receiving the low-frequency protocol (LFS, 2-Hz APs train for 40 s). Bottom: Representative averaged inhibitory post-synaptic currents (IPSCs)—driven by the PV+ interneuron activation—elicited before and 30 min after the LFS, as schematized above.

(B) Potentiation of IPSC amplitude (iLTP) after LFS (arrow; n = 33 neurons, $F_{38,875} = 5.9$, $p < 0.001$, one-way ANOVA followed by Tukey's multiple comparison test).

(C) Top: Experimental configuration including an excitatory hippocampal neuron (gray) receiving the LFS. The "target" symbol indicates an individual GABAergic synapse where DPNI-GABA was uncaged (see STAR Methods). Inset: Representative dendritic portion of a neuron expressing EGFP (green), with GABAergic synapses identified by live labeling of vGAT (red, see STAR Methods). Scale bar, 1 µm. Bottom: Representative averaged traces of uIPSCs before (baseline) and 30 min after LFS (iLTP) as schematized above.

(D) uIPSCs are potentiated after LFS (n = 30 synapses from nine neurons; $F_{4,120} = 6.3$, $p < 0.001$; one-way ANOVA followed by Tukey's multiple comparison test).

(E) CaMKII is required for LFS-induced iLTP. uIPSC amplitude normalized to baseline values in the presence of KN-93 (white; n = 19 synapses from five neurons; $F_{4,64} = 1.6$, $p > 0.05$, one-way ANOVA followed by Tukey's post-test) and the inactive analog KN-92 (pink; n = 26 synapses from seven neurons; $F_{4,92} = 6.5$, $p < 0.001$; one-way ANOVA followed by Tukey's post-test).

(F) Influence of voltage-gated calcium channels (VGCCs) on iLTP expression. Relative (after/before) uIPSC amplitude upon LFS in control conditions (black; n = 46 synapses from 14 neurons; $F_{4,144} = 10.2$, $p < 0.001$), or in the presence of the following VGCCs blockers: ω-conotoxin MVIIC for P/Q and N-type (blue; n = 16 synapses from four neurons; $F_{4,64} = 9.1$, $p < 0.001$), or nifedipine for L-type (green; n = 35 synapses from nine neurons; $F_{4,120} = 5.8$, $p < 0.001$) or ω-conotoxin GVIA for N-type (purple; n = 69 synapses from 16 neurons; $F_{4,205} = 11.5$, $p < 0.001$) or nifedipine and ω-conotoxin MVIIC (orange; n = 24 synapses from six neurons; $F_{4,80} = 0.3$, $p > 0.05$) or nifedipine and ω-conotoxin GVIA (yellow; n = 17 synapses from six neurons; $F_{4,52} = 1.9$, $p > 0.05$). All statistical comparisons were performed with one-way ANOVA followed by Tukey's multiple comparison test. Values are expressed as mean ± SEM. $^{**}p < 0.01$, $^{***}p < 0.001$, ns = not significant. See also Figure S1.

and reveal that this functional interplay is restricted to dendritic microdomains.

## RESULTS

### Electrophysiological induction of inhibitory long-term potentiation

We first sought to identify an electrical stimulation protocol to postsynaptically induce iLTP on cultured hippocampal neurons. To this end, we tested different non-Hebbian depolarization protocols delivered through the patch pipette on a putative excitatory hippocampal neuron and recorded inhibitory post-synaptic currents (IPSCs) elicited by the activation of a connected presynaptic parvalbumin-positive interneuron (PV+) (presynaptic neuron) (Figure 1A). In this paired-patch configuration, the delivery of a 40-s action potential (AP) train at 2 Hz (low-frequency stimulation, LFS) to the excitatory neuron induced a robust increase of IPSCs amplitude (1.34 ± 0.01 fold increase, $p < 0.001$; Figure 1A bottom and 1B). We next investigated whether this form of iLTP was expressed on the pre- or post-synaptic side. First, the amplitude ratio between two consecutive IPSCs elicited at a 50-ms interval (paired-pulse ratio) was unchanged by the LFS protocol (Figure S1A), suggesting a postsynaptic expression mechanism. Moreover, the nitric oxide synthase blocker L-NAME was unable to prevent the LFS-induced iLTP (Figure S1B), thus making a presynaptic mechanism based on nitric oxide-induced increase of GABA release (Guevara-Guzman et al., 2002; Lourenço et al., 2014; Saransaari and Oja, 2006; Xue et al., 2011) unlikely.

We also found that the inclusion of the calcium chelator BAPTA in the patch pipette prevented the IPSC amplitude increase (Figure S1C), indicating that this iLTP depends on the elevation of intracellular calcium following delivery of the post-synaptic LFS. However, blocking NMDA receptors or L-type voltage-gated calcium channels (VGCCs) by APV or nifedipine did not prevent the LFS-dependent increase in GABAergic currents (Figures S1D–S1E). Likewise, co-application of APV and nifedipine failed to inhibit iLTP (Figure S1F). Worth noting, additional potential sources of calcium influx mediated by N-, P/Q-, and R-type VGCC (also expressed presynaptically) were not investigated in these paired-patch configuration experiments, since their blockade could affect GABA release and the amplitude of IPSCs, thus masking their role in iLTP induction.

We corroborated the postsynaptic expression of this LFS-induced iLTP by UV laser uncaging of DPNI-GABA at dendritic

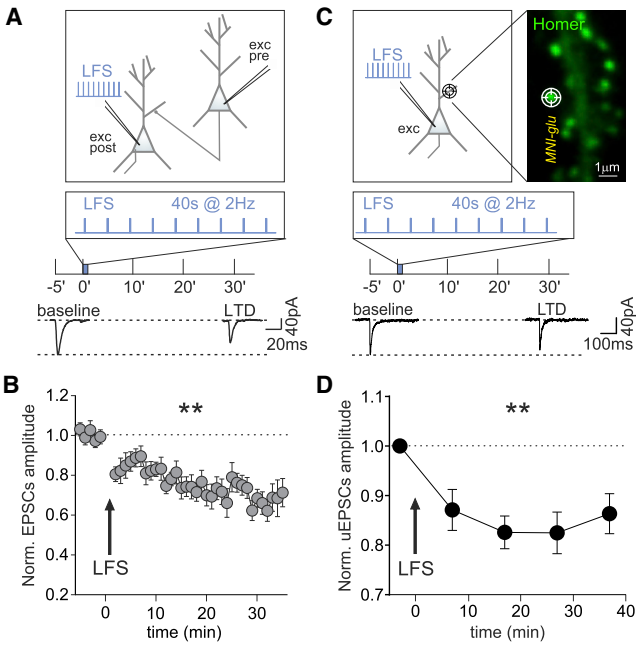


**Figure 2. iLTP-inducing protocol promotes LTD at excitatory synapses**

(A) Top: Experimental configuration of paired-patch recordings of two connected excitatory hippocampal neurons. LFS was delivered to the postsynaptic neuron. Bottom: Representative averaged traces of excitatory postsynaptic response (EPSCs) before and 30 min after the LFS, as depicted above.

(B) Depression of EPSC amplitude (LTD) after LFS (arrow) (n = 5 neurons, $F_{38,726} = 4.2$, $p < 0.001$, one-way ANOVA followed by Tukey's test).

(C) Top: Experimental configuration of an excitatory neuron receiving the LFS. The target symbol indicates MNI-glutamate uncaging at an individual spine identified by Homer1c-GFP (inset; scale bar, 1 μm). Bottom: Representative averaged traces of uncaging EPSCs (uEPSCs) before (baseline) and 30 min after LFS (LTD), as indicated above.

(D) Persistent reduction of uEPSC amplitude after LFS (n = 16 synapses from 11 neurons, $F_{4,68} = 4.7$, $p < 0.01$; one-way ANOVA followed by Tukey's test). Values are expressed as mean ± SEM. **p < 0.01, ***p < 0.001.

proximal GABAergic synapses on the stimulated excitatory neuron (see STAR Methods) (Figure 1C, top). Consistently with the paired-patch recordings, after the application of the LFS protocol, the amplitude of uIPSCs elicited by DPNI-GABA uncaging was significantly increased (at 27 min: 1.26 ± 0.05 fold increase of baseline, $p < 0.001$; Figure 1C bottom and 1D).

We then investigated whether the activation of CaMKII could be involved in the expression of this form of iLTP. We found that the LFS-induced iLTP was prevented by the application of the CaMKII inhibitor KN-93 (normalized uIPSC amplitude at 27 min: 0.93 ± 0.03, $p > 0.05$), whereas KN-92, an inactive analog of KN-93, left iLTP expression unchanged (normalized uIPSC amplitude at 27 min: 1.17 ± 0.04, $p < 0.001$, Figure 1E). We further investigated whether this iLTP depends on dendritic calcium elevation mediated by the postsynaptic N-, P/Q-, and R-type VGCCs by taking advantage of the uncaging technique, which induces synaptic-like currents without engaging the presynaptic release machinery. In presence of nifedipine (to block the L-type VGCCs), or ω-conotoxin MVIIC (to block the P/Q- and N-type VGCCs), or ω-conotoxin GVIA (to block only N-type VGCCs), we observed iLTP similarly to control conditions without drugs (fold increase of uIPSCs amplitude at 27 min: ctrl = 1.25 ± 0.07, $p < 0.001$; nifedipine = 1.15 ± 0.06, $p < 0.001$; MVIIC = 1.22 ± 0.04, $p < 0.001$; GVIA = 1.21 ± 0.06, $p < 0.001$; Figure 1F). On the contrary, the co-application of nifedipine and ω-conotoxin MVIIC to block L-along with P/Q- and N-type VGCCs abolished the potentiation (0.97 ± 0.04 fold increase, $p > 0.05$; Figure 1F). To further dissect the calcium sources responsible for iLTP induction, we co-applied nifedipine with ω-conotoxin GVIA. The evidence that this condition prevented iLTP upon the delivery of LFS (normalized uIPSC amplitude at 27 min: 0.95 ± 0.04 fold increase, $p > 0.05$; Figure 1F) indicated the concomitant involvement of L- and N-type VGCC, with a negligible role for P/Q-type VGCC. Overall, these results suggest that the LFS protocol promotes the increase of IPSC amplitude via the postsynaptic increase of intracellular calcium concentration through the L- and N-type VGCC and the activation of CaMKII.

## LFS induces long-term depression at glutamatergic synapses

Next, we studied the effects of the aforementioned postsynaptic LFS protocol on the plasticity of glutamatergic synapses. To this end, in a paired-patch configuration between two connected excitatory hippocampal neurons, we elicited a single AP in the presynaptic neuron and recorded the consequent excitatory postsynaptic current (EPSC) in the postsynaptic neuron (Figure 2A). The delivery of the LFS protocol (2 Hz for 40 s) to the postsynaptic neuron was responsible for a persistent and significant reduction of EPSC amplitude (0.72 ± 0.02 fold of baseline, $p < 0.001$, Figure 2B), thus indicating the expression of glutamatergic LTD. To assess whether this LTD was expressed at the postsynaptic level, we photo-released MNI-glutamate at individual glutamatergic synapses identified by overexpressed Homer1c-GFP (Figure 2C). After the LFS, the amplitude of uncaging EPSCs (uEPSCs) was significantly reduced (at 27 min: 0.82 ± 0.04 fold of baseline, $p < 0.01$; Figures 2C and 2D), thus indicating a postsynaptic mechanism. This observation is in line with previous studies demonstrating that LFS (in the range of 0.5–5 Hz) are responsible for glutamatergic LTD (Dudek and Bear, 1992; Malenka and Bear, 2004). Overall, we found that the delivery of non-Hebbian LFS protocols leads to an opposite regulation of the plasticity of excitatory and inhibitory synapses.

## Increase of gephyrin clusters is associated with iLTP expression

We also investigated whether the expression of the aforementioned electrically induced iLTP involves the rearrangement of synaptic gephyrin (Petrini et al., 2014). To this end, we monitored EGFP-gephyrin fluorescence over time at individual clusters before and after the application of the iLTP induction protocol (Figures 3A and 3B). After the LFS, the fluorescence intensity of individual EGFP-gephyrin clusters significantly increased with respect to the baseline values (1.17 ± 0.03 fold increase, $p < 0.001$; Figures 3B and 3C), reflecting a promoted accumulation of synaptic gephyrin during iLTP.

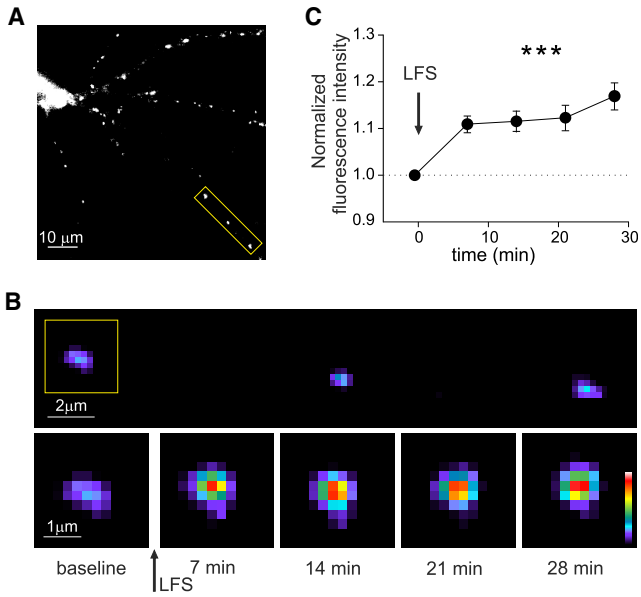


**Figure 3. Enhanced gephyrin clustering during iLTP**

(A) Representative epifluorescence image of a patched neuron expressing EGFP-gephyrin. Scale bar, 10 μm. The LFS protocol (40-s AP trains at 2 Hz) was delivered by patching the neuron. Please note that the fluorescence scale has been enhanced to visualize small clusters.

(B) Top: Pseudocolor magnification of the dendritic portion framed in (A). Scale bar, 2 μm. Bottom: Timelapse of the gephyrin cluster framed above. The arrow indicates LFS. Scale bar, 1 μm.

(C) EGFP-gephyrin fluorescence increases upon iLTP induction with LFS (arrow) ($n = 13$, $F_{4,48} = 21.5$, $p < 0.001$, RM one-way ANOVA followed by Tukey's post-test). Values are expressed as mean ± SEM. ***$p < 0.001$.

## Interaction between plasticity at excitatory and inhibitory synapses

We next included this LFS into a Hebbian protocol, to achieve "single-spine LTP." We paired the 40-s AP train at 2 Hz delivered to a postsynaptic neuron (LFS) with repetitive uncaging of MNI-glutamate at 4 Hz an individual glutamatergic spine on the same neuron (Figure 4A, STAR Methods). As such, we could achieve a Hebbian stimulation where the postsynaptic depolarization (obtained with the LFS) is concomitant with the presynaptic glutamate release at a specific input (mimicked by glutamate uncaging) (Harvey and Svoboda, 2007; Matsuzaki et al., 2004). In a typical experimental layout, we considered two glutamatergic and three GABAergic synapses chosen at different relative distances on the same dendrite (Figure 4A). We found that the delivery of the single-spine LTP protocol (Figure 4A, top) selectively increased the amplitude of uEPSCs elicited at the photo-stimulated spine (Figures 4A and 4B, red).

We next studied GABAergic synapse function upon the induction of single-spine LTP. GABAergic synapses located at distance >3 μm from the photo-stimulated spine were potentiated (iLTP) (Figures 4A, 4C and S2B, normalized uIPSC amplitude: 1.20 ± 0.06 of baseline, $p < 0.001$). Intriguingly, GABAergic synapses located in the close vicinity of the potentiated spine (<3 μm) were depressed (iLTD) (Figures 4C, 4D, and S2B, normalized uIPSC amplitude: 0.85 ± 0.04 of baseline, $p < 0.001$). This suggests that the sign of inhibitory synaptic plasticity depends on the distance of the GABAergic synapse from the potentiated spine (Figure 4D, green, $p < 0.001$) and that the LTP of an individual glutamatergic spine generates a region of reduced inhibition in the spatial range of ± 3μm. Of note, upon the induction of single-spine LTP, other nearby non-photo-stimulated spines remained unaffected, whereas those located more distantly were depressed (Figures 4B and S2A). This plasticity pattern (i.e., iLTP and concomitant LTD) in dendritic regions far from the stimulated spine matches that obtained at GABAergic and glutamatergic synapses by the non-Hebbian delivery of LFS shown in Figures 1 and 2.

In another set of experiments, we observed that the blockade of L-type VGCC prevented local GABAergic iLTD at distances <3 μm from the potentiated spine and reverted it to iLTP, while leaving the iLTP at distance >3 μm unaffected (Figure 4D, purple, Figure S2D). As a control, we assessed that nifedipine did not affect the expression of single-spine LTP (Figure S2C).

Overall, we demonstrate that, while the application of LFS elicits diffuse iLTP, the pairing of LFS with MNI-glutamate uncaging at individual spines induces single-spine LTP and determines a local iLTD restricted to a range of 3 μm from the potentiated glutamatergic spine. Notably, this local iLTD as well as the depression of glutamatergic synapses depend on calcium entry through L-type VGCC.

## Calcium dynamics during the induction of excitatory and inhibitory plasticity

Subsequently, we addressed the spatial and temporal profile of dendritic calcium transients induced by either postsynaptic LFS protocol (non-Hebbian stimulation) or LFS paired with MNI-glutamate uncaging to induce single-spine LTP (Hebbian stimulation) by filling Homer1c-GFP-positive neurons with the synthetic calcium indicator Rhod-2 through the patch pipette (Figure 5A). In response to 10 s of the LFS protocol, calcium rapidly increased and reached a plateau after approximately 3–5 s (Figure 5B black). Similarly, during the 4-Hz train of MNI-glutamate uncaging, dendritic calcium increased at individual glutamatergic spines (Figure 5B, pink). However, the pairing of the LFS with MNI-glutamate uncaging induced an overall calcium increase that was considerably higher than that obtained by either protocol, reaching a plateau after ~5 s (Figure 5B blue). Next, we found that, while LFS alone induced a calcium increase uniformly along the dendrite (Figures 5C and 5D), the delivery of LFS + MNI-glutamate uncaging elicited a further calcium increase that peaked at the photo-stimulated spine (Figures 5C and 5D) and declined back to the calcium levels induced by LFS within a few micrometers (relative fluorescence intensity below the spine = 1.55 ± 0.15, $p < 0.01$, Figure 5E). Importantly, such a range of confined dendritic calcium increase was on par with the spread of the local iLTD (±3 μm, Figure 4D) upon the induction of single-spine LTP. This finding supports the hypothesis that the spatially limited calcium increase in the vicinity of a potentiated glutamatergic spine induced by the Hebbian paired stimulation might lead to the confined expression of iLTD. In this regard, the evidence that such local iLTD is prevented by nifedipine (Figure 4D) suggests the contribution of the L-type VGCC to the calcium increase nearby the potentiated spine. To test this possibility, we studied the effects of nifedipine on dendritic calcium dynamics (Figures

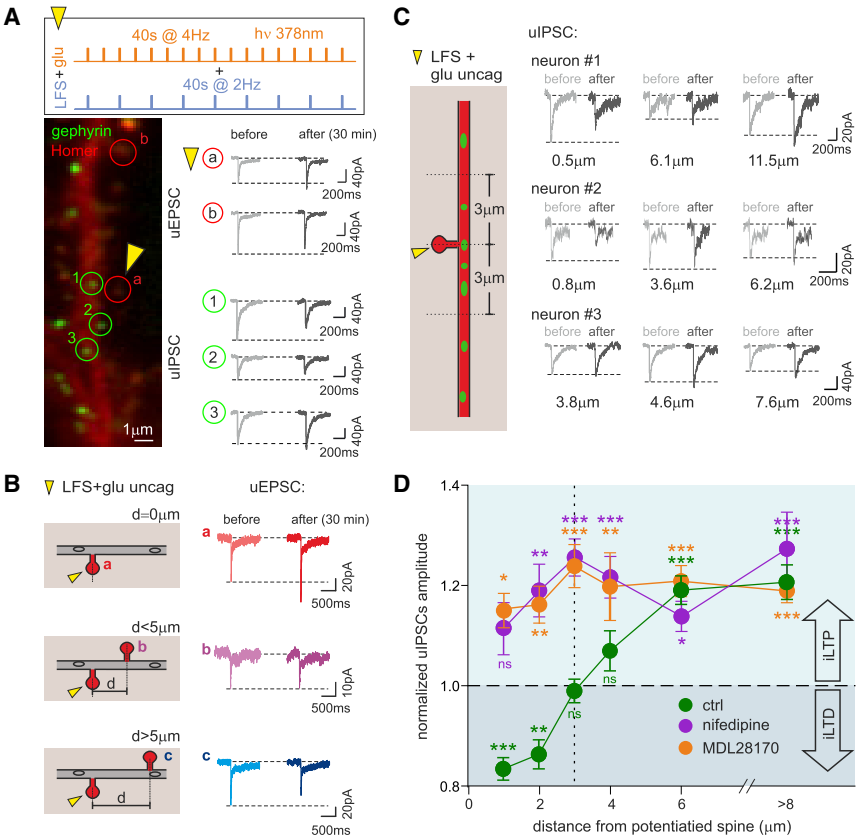


**Figure 4. Plasticity interplay between potentiated spine and neighboring GABAergic synapses**

(A) Top: Schematic representation of the single-spine LTP protocol (yellow arrowhead), showing a 40-s diffraction-limited MNI-glutamate uncaging (glu) with 378-nm light at 4 Hz at an individual spine paired with 40-s APs train at 2 Hz (LFS) delivered to the whole neuron through the patch pipette. Bottom: Representative experiment showing the imaging (left) and the double uncaging electrophysiology (right) performed on the same neuron. Left: Epifluorescence image of a dendritic portion of a neuron expressing Homer1c-DsRed (red) and EGFP-gephyrin (green). Circles indicate individual excitatory (red) and inhibitory (green) synapses probed by uncaging MNI-glutamate and DPNI-GABA, respectively, at different distances from the potentiated spine (yellow arrowhead). Scale bar, 1 μm. Right: Representative averaged traces of uEPSCs and uIPSCs recorded from the circled glutamatergic and GABAergic synapses on the left before and 30 min after the delivery of the single-spine LTP protocol.

(B) Left: Spines at different distances (D) from the stimulated one (arrowhead) are indicated with a, b, and c letters. Right: Representative averaged traces of uEPSCs recorded from glutamatergic synapses as indicated on the left, before and 30 min after the induction of single-spine LTP.

(C) Example traces of uIPSCs recorded before and 30 min after the single-spine LTP protocol. The distance of each GABAergic synapse from the potentiated spine is noted below each trace.

(D) Spatial distribution of GABAergic plasticity of inhibitory synapses located at different distances from the potentiated spine (green, each data point represents at least 22 synapses (max 40) from 21 neurons, $F_{6,232} = 32.6$, $p < 0.001$, one-way ANOVA followed by Tukey's post-test). In the presence of nifedipine or the calpain inhibitor MDL28170, the same protocol (LFS + MNI-glutamate uncaging) fails to elicit iLTD at synapses within 3 μm from the stimulated spine. Nifedipine (purple): each data point represents at least n = 7 (max 16) synapses from seven neurons, $F_{6,68} = 6.6$, $p < 0.001$, one-way ANOVA followed by Tukey's post-test. MDL28170 (orange): each data point represents at least n = 9 (max 67) synapses from 24 neurons, $F_{6,223} = 13.0$, $p < 0.001$, one-way ANOVA followed by Tukey's post-test). Values are expressed as mean ± SEM.*$p < 0.05$, **$p < 0.01$, ***$p < 0.001$, ns = not significant. See also Figure S2.

S3A and S3B). We found that, in the presence of nifedipine, the pairing of LFS with MNI-glutamate uncaging still elicited an increase of calcium with respect to that induced by LFS alone (Figures S3C and S3D). However, nifedipine markedly attenuated the calcium increase nearby the photo-stimulated spine (Figures S3E and S3F), thus indicating that, following Hebbian stimulations, local calcium increase mediated by L-type VGCC activity contributes to the expression of the iLTD observed in the proximity of the potentiated spine.

We next explored the possibility that calpains, a family of calcium-dependent proteases, could be involved in local iLTD. To test this possibility, we interfered with calpain activity by treating neurons with the calpain inhibitor MDL 28170 before the induction of single-spine LTP and studied the synaptic plasticity of inhibitory synapses while considering their distance from the potentiated spine (Figure 4D, orange). For GABAergic synapses close to the potentiated spine (d < 3 μm), not only did they lack the local iLTD observed in control conditions (Figure 4D, compare orange and green), but they in fact exhibited iLTP (at 27 min: uIPSC amplitude = 1.19 ± 0.05 of baseline, $p < 0.001$; Figure S2F). Interestingly, upon calpain blockade, the iLTP expression at inhibitory synapses located at d < 3 μm and at d > 3 μm from the potentiated spine were comparable (Figure 4C orange) (d > 3μm at 27 min: uIPSC amplitude = 1.24 ± 0.04 of baseline, $p < 0.001$; Figure S2F), appearing similar to neurons only exposed to LFS (compare with Figure 1). This suggests that calpain blockade interferes with the confined effects of MNI-glutamate uncaging on inhibitory synaptic plasticity.

## Gephyrin dynamics during the expression of single-spine LTP

Considering that the expression of LFS-induced iLTP involves the promoted clustering of gephyrin at inhibitory synapses (Figure 3), we next investigated whether the converse was true, that is, if the iLTD observed near a potentiated glutamatergic spine is associated with the loss of synaptic gephyrin. We identified gephyrin clusters by means of FingRs (fibronectin intrabodies generated with mRNA display) intrabodies (Gross et al., 2013) fused with GFP to label endogenous gephyrin. While still using GFP signal as a proxy for gephyrin, the intrabodies-based staining procedure significantly reduced gephyrin background fluorescence compared to EGFP-gephyrin overexpression, leading to a higher signal-to-noise ratio that proved essential to satisfactorily detect the mild gephyrin fluorescence reductions

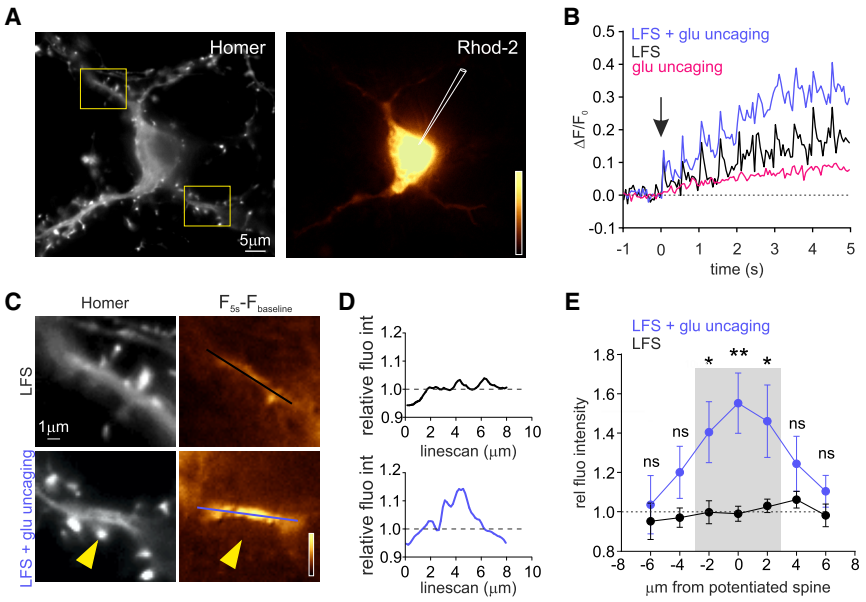


**Figure 5. Spatial dynamics of dendritic calcium during iLTP and LTD**

(A) Representative epifluorescence image of a Homer1c-GFP expressing neuron (left) loaded with Rhod-2 through the patch pipette (gold, right). Scale bar, 5 μm.

(B) Relative Rhod-2 fluorescence intensity quantified during different protocols: LFS (black), LFS paired with glutamate uncaging (blue), and glutamate uncaging alone (pink), in two 4-μm-long dendritic portions of the same neuron. The arrow indicates the beginning of the protocol.

(C) Left: Magnifications of the dendritic portions framed in A, stimulated with LFS (top) or LFS + glutamate uncaging (bottom). The yellow arrowhead indicates the stimulated spine. Scale bar, 1 μm. Right: Gold pseudocolor representation of Rhod-2 fluorescence intensity changes at plateau (5 s) of the stimulating protocols (i.e., LFS, top, and LFS paired with glutamate uncaging, bottom) with respect to baseline values ($F_{5s}$–$F_{baseline}$).

(D) Fluorescence line scans along the lines in C, normalized to the average fluorescence detected along the line scan in LFS.

(E) Changes in the relative dendritic Rhod-2 fluorescence intensity (as measured in Figure 5D) as a function of the distance from a reference or stimulated spine (see STAR Methods). The gray area indicates the range of ± 3μm from the potentiated spine (LFS: n = 23 neurons, LFS + glu uncaging: n = 22 neurons, $F_{1,265}$ = 22.1, p < 0.001, two-way ANOVA followed by Bonferroni's multiple comparison test). Statistical significance for each data point is shown. Values are expressed as mean ± SEM. *p < 0.05, **p < 0.01, ns = not significant. See also Figure S3.

associated with iLTD. Similarly to the experiments shown in Figure 4, we induced single-spine LTP by pairing the LFS protocol with repetitive MNI-uncaging at an individual spine and quantified EGFP fluorescence over time at gephyrin clusters either close (d < 3 μm) or far (d > 3 μm) from the potentiated spine (Figure 6A). We found that after the delivery of the single-spine LTP protocol, gephyrin clusters at d < 3 μm from the potentiated spine were significantly reduced (gephyrin normalized fluorescence intensity = 0.90 ± 0.04 of baseline, p < 0.01; Figure 6B left), whereas at further distances they were increased (gephyrin normalized fluorescence intensity = 1.08 ± 0.04 of baseline, p < 0.05; Figure 6B right). This indicates that the regulation of local gephyrin clustering could underlie the spatial dependence of GABAergic synaptic plasticity, corroborating the match between electrophysiological, calcium imaging, and gephyrin imaging data.

While neuronal cultures represent an ideal model to study the basic features of synapses, it remained to be established whether the paradigm of GABAergic plasticity documented here in cultured hippocampal neurons is conserved in more integrated preparations. To this end, we studied acute hippocampal slices from transduced brains of juvenile mice after injection of AAV-expressing teal fluorescent protein fused to gephyrin (Teal-gephyrin) previously shown to efficiently incorporate at functional inhibitory postsynaptic densities (Chen et al., 2012; Villa et al., 2016) (see STAR Methods). We focused on the dendrites of granule cells (GCs) in the dentate gyrus (DG) that mainly receive excitatory inputs from entorhinal cortex and mossy cells as well as inhibitory inputs from different subclasses of interneurons (Hainmueller and Bartos, 2020). In the GCs proximal apical dendrites (at ∼ 30 μm from the soma), we visualized spines by filling neurons with Alexa 647 through the patch pipette and GABAergic synapses by the fluorescence of Teal-gephyrin clusters (Figure 6C). We found that the density of dendritic Teal-gephyrin puncta (2.39 ± 0.14 per 10 μm) closely matched that observed in previous works exploiting fluorescent proteins fused to gephyrin (either in transgenic mice or overexpressed) to identify GABAergic synapses in *in vivo* and *ex vivo* studies (Chen et al., 2012; Iascone et al., 2020; Villa et al., 2016; Vlachos et al., 2013). To investigate the differential GABAergic synaptic plasticity in relation to the distance from the potentiated spine in slices analogous to our experiments in primary neuronal cultures, we delivered an LFS protocol paired with two-photon MNI-glutamate uncaging at an individual spine to induce single-spine LTP, and subsequently we studied the changes of Teal-gephyrin puncta in the nearby dendritic regions. Of note, the stimulation protocol previously used in hippocampal cultures (LFS + MNI-glutamate uncaging at 4 Hz) was only partially effective in inducing single-spine LTP in hippocampal slices. Therefore, we adjusted the single-spine LTP protocol by increasing the frequency of MNI-glutamate uncaging from 4 to 50 Hz. As such, by pairing LFS with MNI-glutamate uncaging at 50 Hz, we successfully elicited single-spine LTP in GCs, thus identifying a reliable single-spine LTP protocol in hippocampal slices with effects similar to those observed in cultured neurons (Figure 6D). Interestingly, upon the induction of single-spine LTP in acute slices, gephyrin clusters were spatially regulated as indicated by the differential changes in their fluorescence intensity at increasing distances from the stimulated spine (Figure 6E). More specifically, after this single-spine LTP protocol, the fluorescence intensity of Teal-gephyrin clusters located within 4 μm from the potentiated spine decreased (see STAR Methods) (0.85 ± 0.05 fold decrease, n = 6, p < 0.01, Figures 6F and 6G left), whereas

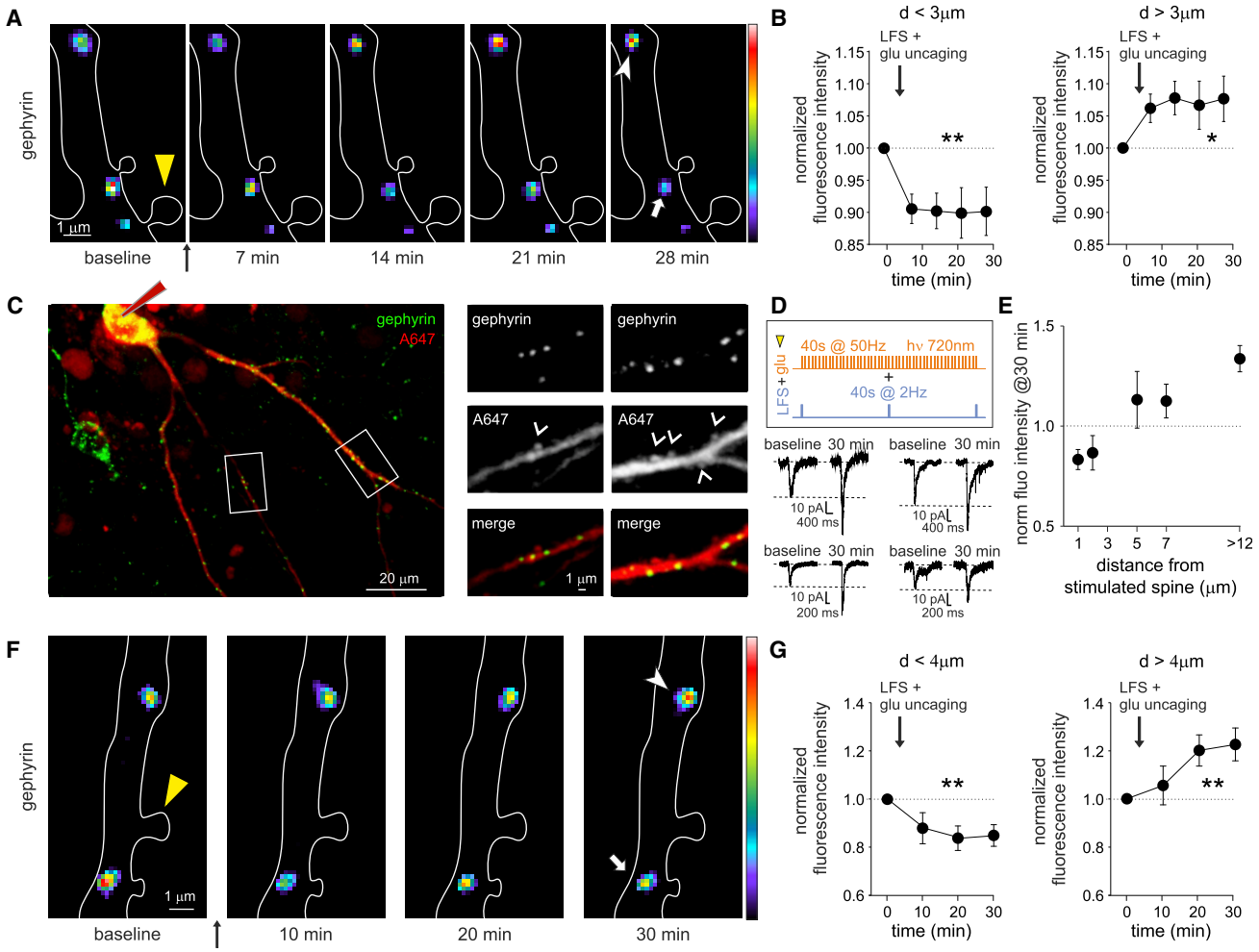


**Figure 6. Gephyrin dynamics after single-spine LTP protocol**

(A) Representative timelapse of pseudocolored FingR-gephyrin-GFP clusters in a dendritic portion of a Homer1c-DsRed$^{+}$ cultured neuron (white outline). Yellow arrowhead: stimulated spine (LFS + uncaging). White arrowhead: a potentiated cluster at d > 3 µm from the stimulated spine. White arrow: depressed cluster at d < 3 µm. Scale bar, 1 µm.

(B) Gephyrin fluorescence intensity is depressed in clusters at d < 3µm from the stimulated spine (n = 13, $F_{4,48} = 4.8$, $p < 0.01$, RM one-way ANOVA followed by Tukey's post-test) (left panel) and potentiated in clusters at d > 3µm (n = 13; $F_{4,48} = 2.7$, $p < 0.05$, RM one-way ANOVA followed by Tukey's post-test) (right panel). Data are presented as mean ± SEM. *p < 0.05, **p < 0.01.

(C) Left: Representative confocal image (z stack projection) of an acute slice of a patched Teal-gephyrin$^{+}$ (green) neuron filled with Alexa Fluor 647 (A647, red). Scale bar, 20µm. Right: magnification of the two dendritic portions framed on the left, showing gephyrin clusters, spines (arrowhead), and the merge of the two channels. Scale bar, 1µm.

(D) Top. Schematics of the single-spine LTP protocol in acute slices. Bottom. Multiple representative averaged traces of uEPSCs recorded from stimulated spines before and 30 min after the protocol.

(E) Differential changes in the fluorescence intensity of gephyrin clusters, depending on the distance from the stimulated spine. Each data point represents at least three synapses (max 5) from six neurons in six slices, $F_{5,17} = 6.7$, $p < 0.01$, one-way ANOVA followed by Tukey's post-test).

(F) Representative confocal image of a dendritic portion of a Teal-gephyrin$^{+}$ neuron (white outline) in acute slice, showing pseudocolored Teal-gephyrin clusters at different time points before (baseline) and after the delivery of the single-spine protocol (yellow arrowhead). White arrowhead: potentiated cluster at d > 4 µm from the stimulated spine. White arrow: depressed clusters at d < 4 µm. Scale bar, 1 µm.

(G) Gephyrin fluorescence intensity is depressed in clusters at d < 4 µm from the stimulated spine (n = 6, $F_{3,15} = 5.5$, $p < 0.01$, RM one-way ANOVA followed by Tukey's post-test) and potentiated at d > 4 µm (n = 6; $F_{3,15} = 6.5$, $p < 0.01$, RM one-way ANOVA followed by Tukey's post-test). Data are presented as mean ± SEM. **p < 0.01.

that of clusters located at > 4 µm from the potentiated spine increased (1.23 ± 0.07 fold increase, n = 6, p < 0.01, Figures 6F and 6G right). Overall, these data indicate that, following the induction of LTP at an individual spine, the clustering of gephyrin is oppositely regulated by the distance from the potentiated spine. In addition, such distance-dependent changes occur both in cultured hippocampal neurons and acute hippocampal brain slices.

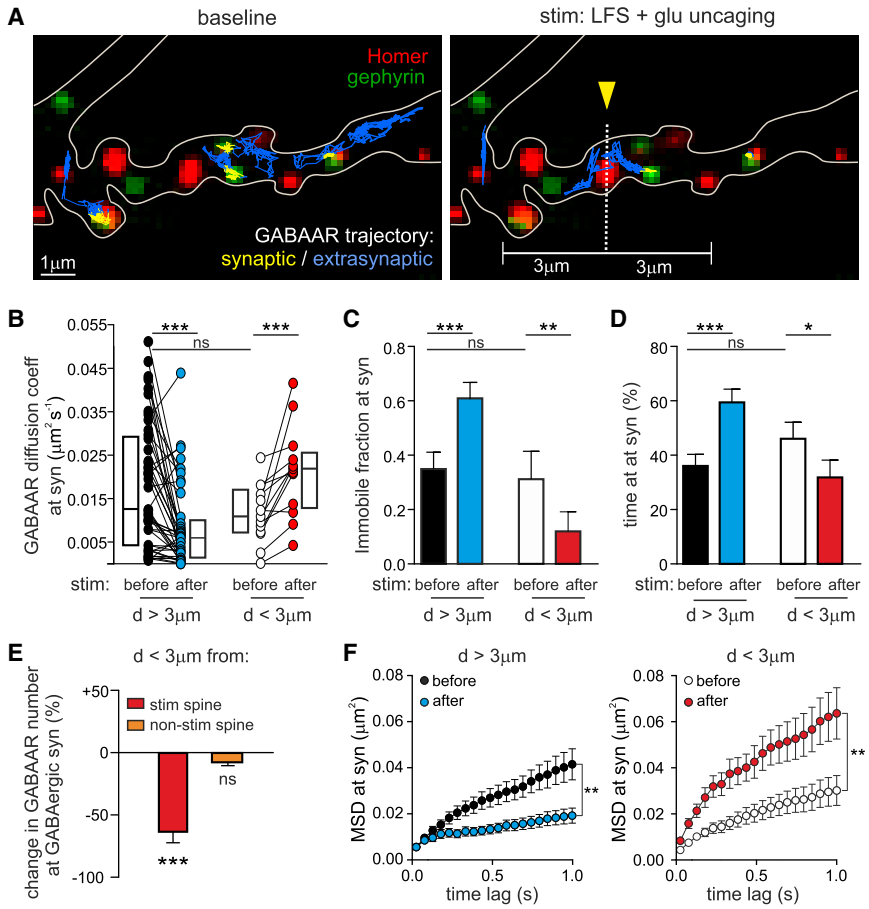


**Figure 7. GABAA receptor lateral diffusion after single-spine LTP protocol**

(A) Representative synaptic (yellow) and extrasynaptic (blue) trajectories of individual GABAARs diffusing on an EGFP-gephyrin$^+$ and Homer1c-DsRed$^+$ neuron, before (left) and after (right) the delivery of the single-spine LTP protocol at the indicated spine (yellow arrowhead). Scale bar, 1 μm.

(B–D). Effect of LFS + glu uncaging on the surface mobility of GABAA receptors at synapses located at d > 3 or d < 3 μm from the potentiated spine.

(B) Paired diffusion coefficient values of synaptic GABAARs (d > 3 μm: n = 45 trajectories from 16 neurons, p < 0.001, Wilcoxon matched-pairs test; d < 3 μm: n = 13 trajectories from nine neurons, p < 0.001, Wilcoxon matched-pairs test). Comparison "before stim" d > 3 μm versus d < 3 μm: p = 0.21, Mann-Whitney test.

(C) Immobile fraction of synaptic GABAARs (d > 3 μm: n = 45 from 16 neurons, p < 0.001, Wilcoxon matched-pairs test; d < 3 μm: n = 13 from nine neurons, p < 0.01, Wilcoxon matched-pairs test). Comparison before d > 3 μm vs d < 3 μm: p > 0.05, Mann-Whitney test.

(D) Percentage of time spent at synapses of synaptic GABAARs (d > 3 μm: n = 45 from 16 neurons, p < 0.001, Wilcoxon matched-pairs test; d < 3 μm: n = 13 from nine neurons, p < 0.05, Wilcoxon matched-pairs test. Comparison "before stim" d > 3 μm versus d < 3 μm: p > 0.05, Mann-Whitney test.

(E) Variation in the number of GABAARs at GABAergic synapses close (d < 3 μm) to the potentiated spine (red; n = 31 from 24 neurons, p < 0.001, Wilcoxon test) or to a spine receiving the same protocol in the absence of MNI-glutamate (orange; n = 48 from 17 neurons, p > 0.05, Wilcoxon test).

(F) MSD versus time values of matched observations of individual GABAARs localized at d > 3μm (left) and d < 3μm (right) from the potentiated spine, before and after LFS + glu uncaging (d > 3 μm: n = 27 from 12 neurons, $F_{1,52} = 8.7$, p < 0.01; d < 3 μm: n = 12 from nine neurons, $F_{1,22} = 9.1$, p < 0.001; RM two-way ANOVA followed by Bonferroni's multiple comparison test). Unless otherwise stated, values are expressed as mean ± SEM.*p < 0.05, **p < 0.01, ***p < 0.001, ns = not significant. See also Figure S4.

## Surface dynamics of GABA receptors after induction of single-spine LTP

We next aimed to understand whether the opposing gephyrin modifications at increasing distances from a single spine expressing LTP are accompanied by differential surface dynamics of GABAA receptors (GABAARs). For this purpose we performed quantum dot (QD)-based single-particle tracking (SPT) (see STAR Methods) and studied the mobility of synaptic GABAAR at inhibitory synapses located either at a distance of ±3 μm from an individual potentiated glutamatergic spine or further away, before and after the expression of single-spine LTP (Figure 7A). Interestingly, at inhibitory synapses located >3 μm from the potentiated spine—that is, those exhibiting iLTP (Figures 4B and S2B)—GABAARs were less mobile after the stimulating protocol, indicated by a reduced paired diffusion coefficient (before = 0.013 $\mu m^2 s^{-1}$ and interquartile range (IQR) 0.004–0.029; after = 0.006 $\mu m^2 s^{-1}$ and IQR: 0.001–0.010; p < 0.001; Figure 7B), an increased immobile fraction (before = 0.35 ± 0.06; after = 0.61 ± 0.06; p < 0.001; Figure 7C), and prolonged time spent at synapses (before = 37% ± 4%; after = 60% ± 5%; p < 0.001; Figure 7D). We next considered GABAARs diffusing at synapses within a 3-μm range from the potentiated spine (d < 3 μm). Before the protocol, they exhibited diffusive properties comparable to more distant GABAARs (p > 0.05; Figures 7B–7D). After the stimulation, those GABAARs close to the potentiated spine (d < 3 μm) (i.e., exhibiting iLTD in response to the single-spine LTP protocol, see Figures 4B and S2B) displayed markedly increased mobility (Figure 7A) as quantified in the diffusion coefficient (before = 0.011 $\mu m^2 s^{-1}$ and IQR: 0.007–0.017; after = 0.022 $\mu m^2 s^{-1}$ and IQR: 0.013–0.026; p < 0.001; Figure 7B), immobile fraction (before = 0.31 ± 0.10; after = 0.12 ± 0.07, p < 0.01; Figure 7C) and reduced time at synapse (before = 0.46 ± 0.06; after = 0.32 ± 0.06; p < 0.05; Figure 7D) after the stimulation. As expected, in these conditions of increased mobility, GABAARs escaped more frequently from the synaptic area, thus depleting inhibitory synapses of GABAARs during local iLTD (−63% ± 9%; p < 0.001; Figure 7E). As a control, we quantified the fraction of residual GABAARs at synapses within 3 μm of non-photo-stimulated spines at the end of each experiment (−7% ± 3%, n = 17; p > 0.05; Figure 7E). The negligible variation in synaptic GABAAR number in this control suggests that GABAARs selectively disperse from inhibitory synapses during local iLTD. Moreover, the few GABAARs that remained at synapses during

iLTD spent less time in that compartment after single-spine LTP induction (before = 46% ± 6%; after = 32% ± 6%; $p < 0.05$; Figure 7D). In line with these data, following the single-spine LTP protocol, the steady state of the mean-square displacement versus time curve (MSD) for GABAARs at synapses far from the potentiated spine ($d > 3$ μm) was reduced, thus indicating higher receptor confinement ($p < 0.01$; Figure 7F, left). In contrast, after the delivery of the same plasticity induction protocol, GABAARs in the dendritic range of ±3 μm from the potentiated spine were less confined, as indicated by an increased MSD steady state ($p < 0.01$; Figure 7F, right).

It is worth noting that the single-spine LTP protocol did not change the lateral diffusion properties of extrasynaptic receptors at distances >3 μm (Figures S3A and S3B). Likewise, matched observations of individual extrasynaptic GABAARs in the range of 3 μm ($d < 3$ μm) from the potentiated spine showed unchanged diffusion coefficients and immobile fractions before and after the single-spine LTP protocol (Figures S3C and S3D), while the percentage of time spent at the extrasynaptic domain increased (Figure S3C right). Control experiments in which the same protocol was performed without puffing MNI-glutamate (i.e., LFS paired with UV illumination) ruled out that the effect of the single-spine LTP protocol on GABAAR diffusion depended on UV laser illumination, but instead required MNI-glutamate uncaging (Figure S4). Overall, these results show that following the induction of single-spine LTP, the spatial dependence of dendritic lateral diffusion of GABAAR faithfully corresponds with modulation of IPSC amplitude and gephyrin synaptic clustering.

## DISCUSSION

In the present study, we reveal that the expression of LTP at individual glutamatergic spines induced by a Hebbian plasticity induction protocol (postsynaptic LFS paired with repetitive MNI-glutamate uncaging) reduces the strength of neighboring GABAergic synapses (local iLTD). In contrast, the delivery of a non-Hebbian protocol (postsynaptic LFS alone) determines the expression of LTD at excitatory synapses and the non-spatially restricted potentiation of inhibitory synapses (iLTP).

Postsynaptic LFS alone, responsible for non-spatially restricted iLTP, elicits a homogeneous dendritic calcium increase that is likely sustained by back-propagating APs. Pairing LFS with repetitive MNI-glutamate uncaging, responsible for the local iLTD, induces a further dendritic calcium increase within 3–4 μm of the stimulated spine. The heavy filtering of synaptic potentials by the spine neck (Yuste, 2013) and the rapid calcium extrusion/buffering at the spine (Sabatini et al., 2002) are expected to largely compartmentalize calcium at spines. However, in line with previous study, our data indicate that the repetitive spine activation (at 4 or 50 Hz) used in the single-spine LTP protocol is sufficient to induce a calcium increase in the parent dendrite (Magee et al., 1995).

Previous works at GABAergic synapses show that sustained calcium influx leads to synaptic depression (Bannai et al., 2009, 2015; Muir et al., 2010), while mild calcium entry determines potentiation (Chiu et al., 2018; Marsden et al., 2007, 2010; Petrini et al., 2014). This indicates that GABAergic plasticity might follow an opposite calcium rule to that of glutamatergic synapses, where high and low intracellular calcium rises have been linked to expression of LTP and LTD, respectively (Coultrap et al., 2014; Lisman, 2001). Thus, a possible explanation for the paradigm of GABAergic plasticity expression shown here is that LFS alone (responsible for mild calcium entry and LTD) can induce iLTP, while the summation of calcium increases due to the pairing of LFS with single-spine MNI-glutamate uncaging would locally induce high calcium concentrations, sufficient to reach the threshold for iLTD (and concomitant LTP). Along the same line, the immobilization or the increased diffusion of synaptic GABAARs correlated with iLTP or iLTD, respectively, consistently with previous work demonstrating that sustained calcium entry increases GABAAR mobility, while moderate calcium entry reduces it (Bannai et al., 2015; Petrini et al., 2014; Petrini and Barberis, 2014; Muir et al., 2010).

We show that the expression of iLTP or iLTD is associated with reduced or enhanced gephyrin clustering, in line with the notion that gephyrin accumulation at the iPSD is a proxy for GABAergic plasticity (Bannai et al., 2009; Battaglia et al., 2018; Flores et al., 2015; Tyagarajan et al., 2011; Villa et al., 2016). However, it must be stressed that given the rich diversity of GABAergic synaptic proteins, both the involvement of gephyrin and the mechanisms of plasticity observed here could vary at specific GABAergic synapse subtypes (Chiu et al., 2019; Fritschy et al., 2012; Barberis, 2019; Chiu et al., 2019; Panzanelli et al., 2011; Tyagarajan and Fritschy, 2014).

The main finding of our study—that excitatory plasticity at an individual spine can affect neighboring GABAergic synapses—closely resembles the paradigms of glutamatergic heterosynaptic plasticity, where the induction of plasticity at spines can modulate the synaptic strength of unstimulated neighboring spines (Chater and Goda, 2021). We propose that sustained local calcium concentration at individual spines may activate calpain in the spine and/or the parent dendrite. In turn, calpain could promote the expression of local iLTD through the proteolysis of gephyrin and the consequent destabilization of the iPSD (Costa et al., 2016; Tyagarajan et al., 2013).

Such a short-range crosstalk mechanism involving biochemical signaling is analogous to what is observed in several forms of heterosynaptic glutamatergic plasticity. For instance, the potentiation of an individual spine can facilitate LTP induction at neighboring spines through the diffusion of h-Ras, RhoA, and Rac1 (Harvey et al., 2008; Hedrick et al., 2016; Murakoshi et al., 2011), while a Ras-ERK pathway is responsible for the increase in AMPA receptor exocytosis near a potentiated spine (Patterson et al., 2010). Similarly, the Hebbian potentiation of a spine in visual cortex (V1) neurons *in vivo* achieved by pairing visual stimuli with optogenetic activation leads to the depression of neighboring spines, mediated by Arc expression (El-Boustani et al., 2018). In addition, calcineurin mediates the shrinkage of unstimulated spines located near multiple potentiated spines (Oh et al., 2015). Interestingly, many forms of heterosynaptic plasticity occur within 3–10 μm (Harvey and Svoboda, 2007; Hedrick et al., 2016; Murakoshi et al., 2011; Oh et al., 2015; Patterson et al., 2010), a distance comparable to that in our synaptic crosstalk, where the local iLTD occurs at GABAergic synapses within 3–4 μm of the potentiated spine.

The coordinated plasticity of excitatory and inhibitory synapses has been tackled previously by investigating populations of

both glutamatergic and GABAergic synapses. In visual cortex pyramidal neurons *in vivo* following monocular deprivation, analyzing the dynamics of spines and GABAergic synapses over a timescale of days has shown that plastic changes are clustered in dendritic sub-regions of ~10 μm (Chen et al., 2012). More recently, Field et al. (2020) applied spike time-dependent plasticity protocols to induce homosynaptic plasticity at multiple synaptic inputs and analyzed the synaptic plasticity changes at unstimulated inputs. Interestingly, heterosynaptic plasticity, mediated by calcium-induced calcium release, efficiently normalized the excitation-to-inhibition (E/I) balance on a timescale of minutes through the coordinated plasticity of glutamatergic and GABAergic synaptic inputs. Our study reveals the spatial rules of heterosynaptic inhibitory plasticity, thus providing essential knowledge for an overarching mechanistic framework for the fine-scale topology of dendritic GABAergic synaptic remodeling in response to the expression of glutamatergic homosynaptic plasticity.

We show that non-Hebbian and Hebbian stimulations oppositely regulate synaptic excitation and inhibition. This result could appear to contrast with a previous study showing that in principle neurons in layer 2/3 of the visual cortex, glutamatergic and GABAergic inputs from PV+ interneurons are remarkably balanced (Xue et al., 2014). However, in our model, local synaptic E/I imbalance could still be equalized if considering larger portions of dendrites or the whole neuron, where equilibrium among the aforementioned opposite plasticity domains could be reached. It also has to be underscored that we studied a subset of glutamatergic and GABAergic synapses located in proximal dendritic regions of cultured hippocampal neuron and DG GCs in hippocampal slices. It is likely that GABAergic inputs located in different regions of the axodendritic axis could show different heterosynaptic plasticity. This might be due to the different relative distances between glutamatergic and GABAergic inputs (Iascone et al., 2020; Megías et al., 2001) or to the intrinsic plasticity of GABAergic synapses formed by specific sub-types of interneurons (Chiu et al., 2018; He et al., 2015; Udakis et al., 2020). In addition, in the present study, we characterize glutamatergic and GABAergic plasticity only in response to postsynaptic LFS combined with glutamate uncaging. For instance, differently from our paradigm, theta burst stimulations (TBS) increase both glutamatergic and GABAergic synapses (Bourne and Harris, 2011; Flores et al., 2015). Recently, an elegant study exploiting optical control of α5-containing GABAARs demonstrated that in hippocampus Schaffer collaterals, the induction of glutamatergic LTP by TBS protocols determined the inclusion of α5-containing GABAARs in the GABAergic PSD, thereby potentiating inhibitory responses (Davenport et al., 2021). These data indicate that diverse stimulation paradigms express specific types of coordinated glutamatergic and GABAergic plasticity.

The heterosynaptic crosstalk characterized here occurs within minutes after the induction of homosynaptic plasticity, and thus likely involves protein redistribution upon biochemical signaling. However, at longer timescales relative to synaptic crosstalk, the synaptic tag and capture theory posits that the inclusion of newly synthesized plasticity-related proteins at tagged synapses stabilizes local synaptic plasticity (Frey and Morris, 1997; Hedrick and Yasuda, 2017; Redondo and Morris, 2011). Thus, the early stage plasticity modifications we observe in our paradigm could subsequently allow the capture of plasticity-related proteins at both excitatory and inhibitory synapses. In this scenario, it would be interesting to clarify whether the local iLTD results from the competition between glutamatergic and GABAergic synapses for the same set of newly synthesized plasticity-related proteins or whether two different sets of proteins selectively stabilize LTP and local iLTD. *In vivo* studies in visual cortex have shown that over several days, GABAergic dendritic synapses can be frequently formed and eliminated in the same location, leading to a new definition of inhibitory synaptic plasticity that relies on substantial, dynamic rearrangements of GABAergic synapses (Chen et al., 2012; Villa et al., 2016). In light of this perspective, it will be important to establish how the synaptic interplay shown here modulates the rate of insertion or elimination of both the glutamatergic and GABAergic spines involved in local plasticity over the long term.

At glutamatergic synapses, the aforementioned mechanisms of synaptic crosstalk promote the convergence of clustered inputs onto specific dendritic sub-regions (Kleindienst et al., 2011; Losonczy et al., 2008; Makino and Malinow, 2011; Takahashi et al., 2012; Zhang et al., 2015), a configuration that is important for the non-linear integration of synaptic signals and the generation of dendritic spikes (Grienberger et al., 2015; Häusser and Mel, 2003; Poirazi and Mel, 2001; Polsky et al., 2004). Such complex dendritic excitability enhances neuronal computational power and information storage (Govindarajan et al., 2011; Lavzin et al., 2012; Wilson et al., 2016; Xu et al., 2012). In addition to glutamatergic signaling, GABAergic synapses play an important role in dendritic computation (Cazé et al., 2014; Tran-Van-Minh et al., 2015). Since the local activation of dendritic GABAA has been shown to downregulate neighboring spines (Hayama et al., 2013), active GABAergic synapses might prevent the formation of clusters of potentiated spines. Thus, the reduction of inhibition of nearby potentiated spines that we show in the present study could represent a key event that reshapes the synaptic ensemble to meet new computation needs.

The synaptic E/I balance has been shown to be altered in neurological disorders (Antoine et al., 2019; Lewis et al., 2012; Rubenstein and Merzenich, 2003). Our study converges toward the hypothesis that E/I could be selectively disrupted in specific dendritic microdomains, even where the overall E/I balance is preserved at the level of the whole neuron. An alteration of heterosynaptic plasticity of glutamatergic and GABAergic synapses in microscale compartments would be well-poised to produce subtle disruptions of dendritic integration and network function. Such mechanisms are expected to be particularly effective in view of the high degree of compartmentalization of both excitatory and inhibitory synaptic inputs in dendritic sub-regions of pyramidal neurons (Klausberger and Somogyi, 2008; Spruston, 2008).

### Limitations of the study

In SPT experiments, individual surface GABAA receptors were tethered to a QD through the binding to a specific primary antibody. Since at the neuronal surface the extrasynaptic receptors markedly outnumber the synaptic ones, it might be objected that the aforementioned procedure would lead to the preferential labeling of extrasynaptic receptors rather than synaptic ones.

However, since receptors constantly diffuse between synaptic and extrasynaptic compartments, receptors initially labeled in the extrasynaptic area will eventually become synaptic. In this regard, we cannot exclude that such receptors might represent a specific sub-population of synaptic receptors.

Another possible limitation of the SPT technique is that the QD-antibody complex could affect the receptor trajectories due to steric hindrance in specific neuronal compartments exhibiting spatial constrains such as, e.g., the synaptic cleft (but see Groc et al., 2007).

We show that the plasticity of excitatory synapses can affect neighboring dendritic inhibitory synapses. However, we did not take into consideration the diversity of GABAergic synapses. Indeed, GABAergic synapses formed by the several sub-classes of inhibitory interneurons might show substantially different interplay rules.

## STAR★METHODS

Detailed methods are provided in the online version of this paper and include the following:

- KEY RESOURCES TABLE
- RESOURCE AVAILABILITY
  - Lead contact
  - Materials availability
  - Data and code availability
- EXPERIMENTAL MODEL AND SUBJECT DETAILS
  - Animals
  - Primary neuronal cultures
  - Acute slices preparation
- METHOD DETAILS
  - Plasmid constructs
  - Transfection and synapse visualization
  - Viral preparation
  - Viral injection
  - Antibodies and drugs
  - Electrophysiological recordings in primary neuronal cultures
  - Electrophysiological recordings in acute hippocampal slices
  - Neurotransmitter uncaging
  - Plasticity induction
  - Live-cell imaging
  - Calcium imaging
  - Quantum dot labelling and imaging
  - Single particle tracking
- QUANTIFICATION AND STATISTICAL ANALYSIS

## SUPPLEMENTAL INFORMATION

Supplemental information can be found online at https://doi.org/10.1016/j.celrep.2022.110347.

## ACKNOWLEDGMENTS

We thank Stefania Guazzi, Mattia Pesce, Andrea Contestabile, and the IIT animal facility for technical help. This work has been supported by Telethon-Italy (GGP11043) and Compagnia di San Paolo (ROL-4318).

## AUTHOR CONTRIBUTIONS

Conceptualization, A.B.; Methodology, T.R., M.R., E.M.P., and A.B.; Validation, T.R., M.R., E.M.P., and A.B.; Formal Analysis, T.R., M.R., E.M.P., and A.B.; Investigation, T.R., M.R., and V.R.; Resources, T.R., M.R., and A.P.; Data Curation, T.R., M.R.; Writing – original Draft, A.B., M.R., and T.R.; Writing – Review & Editing, A.B. and E.M.P.; Visualization, T.R., E.M.P., M.R., A.P., and A.B.; Supervision, A.B.; Project Administration, A.B.; Funding Acquisition, A.B.

## DECLARATION OF INTERESTS

The authors declare no competing interests.

Received: October 4, 2019
Revised: September 16, 2021
Accepted: January 14, 2022
Published: February 8, 2022

## REFERENCES

Andres, A.L., Regev, L., Phi, L., Seese, R.R., Chen, Y., Gall, C.M., and Baram, T.Z. (2013). NMDA receptor activation and calpain contribute to disruption of dendritic spines by the stress neuropeptide CRH. J. Neurosci. *33*, 16945–16960.

Antoine, M.W., Langberg, T., Schnepel, P., and Feldman, D.E. (2019). Increased excitation-inhibition ratio stabilizes synapse and circuit excitability in four autism mouse models. Neuron *101*, 648–661.

Bannai, H., Lévi, S., Schweizer, C., Inoue, T., Launey, T., Racine, V., Sibarita, J.B., Mikoshiba, K., and Triller, A. (2009). Activity-dependent tuning of inhibitory neurotransmission based on GABAAR diffusion dynamics. Neuron *62*, 670–682.

Bannai, H., Niwa, F., Sherwood, M.W., Shrivastava, A.N., Arizono, M., Miyamoto, A., Sugiura, K., Lévi, S., Triller, A., and Mikoshiba, K. (2015). Bidirectional control of synaptic GABAAR clustering by glutamate and calcium. Cell Rep *13*, 2768–2780.

Barberis, A. (2019). Postsynaptic plasticity of GABAergic synapses. Neuropharmacology *169*, 107643.

Battaglia, S., Renner, M., Russeau, M., Côme, E., Tyagarajan, S.K., and Lévi, S. (2018). Activity-dependent inhibitory synapse scaling is determined by gephyrin phosphorylation and subsequent regulation of GABA A receptor diffusion. Eneuro *5*, ENEURO.0203-17.2017. https://doi.org/10.1523/ENEURO.0203-17.2017.

Baudouin, S.J., Gaudias, J., Gerharz, S., Hatstatt, L., Zhou, K., Punnakkal, P., Tanaka, K.F., Spooren, W., Hen, R., De Zeeuw, C.I., et al. (2012). Shared synaptic pathophysiology in syndromic and nonsyndromic rodent models of autism. Science *338*, 128–132.

Bourne, J.N., and Harris, K.M. (2011). Coordination of size and number of excitatory and inhibitory synapses results in a balanced structural plasticity along mature hippocampal CA1 dendrites during LTP. Hippocampus *21*, 354–373.

Briz, V., and Baudry, M. (2017). Calpains: master regulators of synaptic plasticity. Neuroscientist *23*, 221–231.

Carta, M., Opazo, P., Veran, J., Athané, A., Choquet, D., Coussen, F., and Mulle, C. (2013). CaMKII-dependent phosphorylation of GluK5 mediates plasticity of kainate receptors. EMBO J. *32*, 496–510.

Castillo, P.E., Chiu, C.Q., and Carroll, R.C. (2011). Long-term plasticity at inhibitory synapses. Curr. Opin. Neurobiol. *21*, 328–338.

Cazé, R.D., Humphries, M.D., and Gutkin, B.S. (2014). Dendrites Enhance Both Single Neuron and Network Computation (New York, NY: Springer), pp. 365–380.

Chater, T.E., and Goda, Y. (2021). My neighbour hetero — deconstructing the mechanisms underlying heterosynaptic plasticity. Curr. Opin. Neurobiol. *67*, 106–114.

Chen, J.L., Villa, K.L., Cha, J.W., So, P.T.C., Kubota, Y., and Nedivi, E. (2012). Clustered dynamics of inhibitory synapses and dendritic spines in the adult neocortex. Neuron *74*, 361–373.

Chiu, C.Q., Martenson, J.S., Yamazaki, M., Natsume, R., Sakimura, K., Tomita, S., Tavalin, S.J., and Higley, M.J. (2018). Input-specific NMDAR-dependent potentiation of dendritic GABAergic inhibition. Neuron *97*, 368–377.

Chiu, C.Q., Barberis, A., and Higley, M.J. (2019). Preserving the balance: diverse forms of long-term GABAergic synaptic plasticity. Nat. Rev. Neurosci. *20*, 272–281.

Choquet, D., and Triller, A. (2013). The dynamic synapse. Neuron *80*, 691–703.

Collins, T.J., Lipp, P., Berridge, M.J., and Bootman, M.D. (2001). Mitochondrial Ca2+ uptake depends on the spatial and temporal profile of cytosolic Ca2+ signals. J. Biol. Chem. *276*, 26411–26420.

Costa, J.T., Mele, M., Baptista, M.S., Gomes, J.R., Ruscher, K., Nobre, R.J., de Almeida, L.P., Wieloch, T., and Duarte, C.B. (2016). Gephyrin cleavage in in vitro brain ischemia decreases GABAA receptor clustering and contributes to neuronal death. Mol. Neurobiol. *53*, 3513–3527.

Coultrap, S.J., Freund, R.K., O'Leary, H., Sanderson, J.L., Roche, K.W., Dell'Acqua, M.L., and Bayer, K.U. (2014). Autonomous CaMKII mediates both LTP and LTD using a mechanism for differential substrate site selection. Cell Rep *6*, 431–437.

Davenport, C.M., Rajappa, R., Katchan, L., Taylor, C.R., Tsai, M.-C., Smith, C.M., de Jong, J.W., Arnold, D.B., Lammel, S., and Kramer, R.H. (2021). Relocation of an Extrasynaptic GABAA receptor to inhibitory synapses freezes excitatory synaptic strength and preserves memory. Neuron *109*, 123–134.

Diering, G.H., and Huganir, R.L. (2018). The AMPA receptor code of synaptic plasticity. Neuron *100*, 314–329.

Dudek, S.M., and Bear, M.F. (1992). Homosynaptic long-term depression in area CA1 of hippocampus and effects of N-methyl-D-aspartate receptor blockade. Proc. Natl. Acad. Sci. U. S. A. *89*, 4363–4367.

El-Boustani, S., Ip, J.P.K., Breton-Provencher, V., Knott, G.W., Okuno, H., Bito, H., and Sur, M. (2018). Locally coordinated synaptic plasticity of visual cortex neurons in vivo. Science. *360*, 1349–1354.

Field, R.E., D'amour, J.A., Tremblay, R., Miehl, C., Rudy, B., Gjorgjieva, J., and Froemke, R.C. (2020). Heterosynaptic plasticity determines the set point for cortical excitatory-inhibitory balance. Neuron *106*, 842–854.

Flores, C.E., Nikonenko, I., Mendez, P., Fritschy, J.-M., Tyagarajan, S.K., and Muller, D. (2015). Activity-dependent inhibitory synapse remodeling through gephyrin phosphorylation. Proc. Natl. Acad. Sci. *112*, E65–E72.

Frey, U., and Morris, R.G.M. (1997). Synaptic tagging and long-term potentiation. Nature *385*, 533–536.

Fritschy, J.M., Panzanelli, P., and Tyagarajan, S.K. (2012). Molecular and functional heterogeneity of GABAergic synapses. Cell. Mol. Life Sci. *69*, 2485–2499.

Govindarajan, A., Israely, I., Huang, S.-Y., and Tonegawa, S. (2011). The dendritic branch is the preferred integrative unit for protein synthesis-dependent LTP. Neuron *69*, 132–146.

Grienberger, C., Chen, X., and Konnerth, A. (2015). Dendritic function in vivo. Trends Neurosci. *38*, 45–54.

Groc, L., Lafourcade, M., Heine, M., Renner, M., Racine, V., Sibarita, J.-B., Lounis, B., Choquet, D., and Cognet, L. (2007). Surface trafficking of neurotransmitter receptor: comparison between single-molecule/quantum dot strategies. J. Neurosci. *27*, 12433–12437.

Gross, G.G., Junge, J.A., Mora, R.J., Kwon, H.B., Olson, C.A., Takahashi, T.T., Liman, E.R., Ellis-Davies, G.C.R., McGee, A.W., Sabatini, B.L., et al. (2013). Recombinant probes for visualizing endogenous synaptic proteins in living neurons. Neuron *78*, 971–985.

Guevara-Guzman, R., Emson, P.C., and Kendrick, K.M. (2002). Modulation of in vivo striatal transmitter release by nitric oxide and cyclic GMP. J. Neurochem. *62*, 807–810.

Hainmueller, T., and Bartos, M. (2020). Dentate gyrus circuits for encoding, retrieval and discrimination of episodic memories. Nat. Rev. Neurosci. *21*, 153–168.

Harvey, C.D., and Svoboda, K. (2007). Locally dynamic synaptic learning rules in pyramidal neuron dendrites. Nature *450*, 1195–1200.

Harvey, C.D., Yasuda, R., Zhong, H., and Svoboda, K. (2008). The spread of Ras activity triggered by activation of a single dendritic spine. Science *321*, 136–140.

Häusser, M., and Mel, B. (2003). Dendrites: bug or feature? Curr. Opin. Neurobiol. *13*, 372–383.

Hayama, T., Noguchi, J., Watanabe, S., Takahashi, N., Hayashi-Takagi, A., Ellis-Davies, G.C.R., Matsuzaki, M., and Kasai, H. (2013). GABA promotes the competitive selection of dendritic spines by controlling local Ca2+ signaling. Nat. Neurosci. *16*, 1409–1416.

He, Q., Duguid, I., Clark, B., Panzanelli, P., Patel, B., Thomas, P., Fritschy, J.M., and Smart, T.G. (2015). Interneuron- and $GABA_A$ receptor-specific inhibitory synaptic plasticity in cerebellar Purkinje cells. Nat. Commun. *6*, 1–13.

Hedrick, N.G., and Yasuda, R. (2017). Regulation of Rho GTPase proteins during spine structural plasticity for the control of local dendritic plasticity. Curr. Opin. Neurobiol. *45*, 193–201.

Hedrick, N.G., Harward, S.C., Hall, C.E., Murakoshi, H., McNamara, J.O., and Yasuda, R. (2016). Rho GTPase complementation underlies BDNF-dependent homo- and heterosynaptic plasticity. Nature *538*, 104–108.

Iascone, D.M., Li, Y., Sümbül, U., Doron, M., Chen, H., Andreu, V., Goudy, F., Blockus, H., Abbott, L.F., Segev, I., et al. (2020). Whole-neuron synaptic mapping reveals spatially precise excitatory/inhibitory balance limiting dendritic and somatic spiking. Neuron *106*, 566–578.

Ibata, K., Sun, Q., and Turrigiano, G.G. (2008). Rapid synaptic scaling induced by changes in postsynaptic firing. Neuron *57*, 819–826.

Kaiser, K.M.M., Lübke, J., Zilberter, Y., and Sakmann, B. (2004). Postsynaptic calcium influx at single synaptic contacts between pyramidal neurons and bitufted interneurons in Layer 2/3 of Rat neocortex is enhanced by backpropagating action potentials. J. Neurosci. *24*, 1319–1329.

Kano, M., Kano, M., Fukunaga, K., and Konnerth, A. (1996). Ca2+-induced rebound potentiation of γ-aminobutyric acid-mediated currents requires activation of Ca2+/calmodulin-dependent kinase II. Proc. Natl. Acad. Sci. U. S. A. *93*, 13351–13356.

Klausberger, T., and Somogyi, P. (2008). Neuronal diversity and temporal dynamics: the unity of hippocampal circuit operations. Science *321*, 53–57.

Kleindienst, T., Winnubst, J., Roth-Alpermann, C., Bonhoeffer, T., and Lohmann, C. (2011). Activity-dependent clustering of functional synaptic inputs on developing hippocampal dendrites. Neuron *72*, 1012–1024.

Kurotani, T., Yamada, K., Yoshimura, Y., Crair, M.C., and Komatsu, Y. (2008). State-dependent bidirectional modification of somatic inhibition in neocortical pyramidal cells. Neuron *57*, 905–916.

Lavzin, M., Rapoport, S., Polsky, A., Garion, L., and Schiller, J. (2012). Nonlinear dendritic processing determines angular tuning of barrel cortex neurons in vivo. Nature *490*, 397–401.

Lewis, D.A., Curley, A.A., Glausier, J.R., and Volk, D.W. (2012). Cortical parvalbumin interneurons and cognitive dysfunction in schizophrenia. Trends Neurosci. *35*, 57–67.

Lisman, J.E. (2001). Three Ca2+ levels affect plasticity differently: the LTP zone, the LTD zone and no man's land. J. Physiol. *532*, 285.

Losonczy, A., Makara, J.K., and Magee, J.C. (2008). Compartmentalized dendritic plasticity and input feature storage in neurons. Nature *452*, 436–441.

Lourenço, J., Pacioni, S., Rebola, N., van Woerden, G.M., Marinelli, S., DiGregorio, D., and Bacci, A. (2014). Non-associative potentiation of perisomatic inhibition alters the temporal coding of neocortical layer 5 pyramidal neurons. PLoS Biol *12*, 1–19.

de Luca, E., Ravasenga, T., Petrini, E.M., Polenghi, A., Nieus, T., Guazzi, S., and Barberis, A. (2017). Inter-synaptic lateral diffusion of GABAA receptors shapes inhibitory synaptic currents. Neuron *95*, 63–69.

Magee, J.C., Christofi, G., Miyakawa, H., Christie, B., Lasser-Ross, N., and Johnston, D. (1995). Subthreshold synaptic activation of voltage-gated Ca2+ channels mediates a localized Ca2+ influx into the dendrites of hippocampal pyramidal neurons. J. Neurophysiol. *74*, 1335–1342.

Makino, H., and Malinow, R. (2011). Compartmentalized versus global synaptic plasticity on dendrites controlled by experience. Neuron *72*, 1001–1011.

Malenka, R.C., and Bear, M.F. (2004). LTP and LTD: an embarrassment of riches. Neuron *44*, 5–21.

Marsden, K.C., Beattie, J.B., Friedenthal, J., and Carroll, R.C. (2007). NMDA receptor activation potentiates inhibitory transmission through GABA receptor-associated protein-dependent exocytosis of GABAA receptors. J. Neurosci. *27*, 14326–14337.

Marsden, K.C., Shemesh, A., Bayer, K.U., and Carroll, R.C. (2010). Selective translocation of Ca2+/calmodulin protein kinase II (CaMKII ) to inhibitory synapses. Proc. Natl. Acad. Sci. *107*, 20559–20564.

Matsuzaki, M., Honkura, N., Ellis-Davies, G.C.R., and Kasai, H. (2004). Structural basis of long-term potentiation in single dendritic spines. Nature *429*, 761–766.

McClure, C., Cole, K.L.H., Wulff, P., Klugmann, M., and Murray, A.J. (2011). Production and titering of recombinant adeno-associated viral vectors. J. Vis. Exp. *57*, e3348.

Megías, M., Emri, Z., Freund, T.F., and Gulyás, A.I. (2001). Total number and distribution of inhibitory and excitatory synapses on hippocampal CA1 pyramidal cells. Neuroscience *102*, 527–540.

Minta, A., Kao, J.P.Y., and Tsien, R.Y. (1989). Fluorescent indicators for cytosolic calcium based on rhodamine and fluorescein chromophores. J. Biol. Chem. *264*, 8171–8178.

Muir, J., Arancibia-Carcamo, I.L., MacAskill, A.F., Smith, K.R., Griffin, L.D., and Kittler, J.T. (2010). NMDA receptors regulate GABAA receptor lateral mobility and clustering at inhibitory synapses through serine 327 on the 2 subunit. Proc. Natl. Acad. Sci. *107*, 16679–16684.

Mulkey, R.M., Endo, S., Shenolikar, S., and Malenka, R.C. (1994). Involvement of a calcineurin/inhibitor-1 phosphatase cascade in hippocampal long-term depression. Nature *369*, 486–488.

Murakoshi, H., Wang, H., and Yasuda, R. (2011). Local, persistent activation of Rho GTPases during plasticity of single dendritic spines. Nature *472*, 100–104.

Nicoll, R.A., and Roche, K.W. (2013). Long-term potentiation: peeling the onion. Neuropharmacology *74*, 18–22.

Nusser, Z., Sieghart, W., Benke, D., Fritschy, J.M., and Somogyi, P. (1996). Differential synaptic localization of two major $\gamma$-aminobutyric acid type A receptor $\alpha$ subunits on hippocampal pyramidal cells. Proc. Natl. Acad. Sci. U. S. A. *93*, 11939–11944.

Nusser, Z., Hájos, N., Somogyi, P., and Mody, I. (1998). Increased number of synaptic GABAA receptors underlies potentiation at hippocampal inhibitory synapses. Nature *395*, 172–177.

Oh, W.C., Parajuli, L.K., and Zito, K. (2015). Heterosynaptic structural plasticity on local dendritic segments of hippocampal CA1 neurons. Cell Rep *10*, 162–169.

Panzanelli, P., Gunn, B.G., Schlatter, M.C., Benke, D., Tyagarajan, S.K., Scheiffele, P., Belelli, D., Lambert, J.J., Rudolph, U., and Fritschy, J.M. (2011). Distinct mechanisms regulate GABA A receptor and gephyrin clustering at perisomatic and axo-axonic synapses on CA1 pyramidal cells. J. Physiol. *589*, 4959–4980.

Patterson, M.A., Szatmari, E.M., and Yasuda, R. (2010). AMPA receptors are exocytosed in stimulated spines and adjacent dendrites in a Ras-ERK-dependent manner during long-term potentiation. Proc. Natl. Acad. Sci. *107*, 15951–15956.

Pennacchietti, F., Vascon, S., Nieus, T., Rosillo, C., Das, S., Tyagarajan, S.K., Diaspro, A., Del Bue, A., Petrini, E.M., Barberis, A., et al. (2017). Nanoscale molecular reorganization of the inhibitory postsynaptic density is a determinant of GABAergic synaptic potentiation. J. Neurosci. *37*, 1747–1756.

Petrini, E.M., and Barberis, A. (2014). Diffusion dynamics of synaptic molecules during inhibitory postsynaptic plasticity. Front. Cell. Neurosci. *8*, 300.

Petrini, E.M., Lu, J., Cognet, L., Lounis, B., Ehlers, M.D., and Choquet, D. (2009). Endocytic trafficking and recycling maintain a pool of mobile surface AMPA receptors required for synaptic potentiation. Neuron *63*, 92–105.

Petrini, E.M., Nieus, T., Ravasenga, T., Succol, F., Guazzi, S., Benfenati, F., and Barberis, A. (2011). Influence of GABAAR monoliganded states on GABAergic responses. J. Neurosci. *31*, 1752–1761.

Petrini, E.M., Ravasenga, T., Hausrat, T.J., Iurilli, G., Olcese, U., Racine, V., Sibarita, J.B., Jacob, T.C., Moss, S.J., Benfenati, F., et al. (2014). Synaptic recruitment of gephyrin regulates surface GABA A receptor dynamics for the expression of inhibitory LTP. Nat. Commun. *5*, 3921.

Poirazi, P., and Mel, B.W. (2001). Impact of active dendrites and structural plasticity on the memory capacity of neural tissue. Neuron *29*, 779–796.

Polsky, A., Mel, B.W., and Schiller, J. (2004). Computational subunits in thin dendrites of pyramidal cells. Nat. Neurosci. *7*, 621–627.

Rannals, M.D., and Kapur, J. (2011). Homeostatic strengthening of inhibitory synapses is mediated by the accumulation of GABA A receptors. J. Neurosci. *31*, 17701–17712.

Redondo, R.L., and Morris, R.G.M. (2011). Making memories last: the synaptic tagging and capture hypothesis. Nat. Rev. Neurosci. *12*, 17–30.

Rubenstein, J.L.R., and Merzenich, M.M. (2003). Model of autism: increased ratio of excitation/inhibition in key neural systems. Genes, Brain Behav. *2*, 255–267.

Sabatini, B.L., Oertner, T.G., and Svoboda, K. (2002). The life cycle of Ca2+ ions in dendritic spines. Neuron *33*, 439–452.

Saransaari, P., and Oja, S.S. (2006). Modulation of GABA release by second messenger substances and NO in mouse brain stem slices under normal and ischemic conditions. Neurochem. Res. *31*, 1317–1325.

Spruston, N. (2008). Pyramidal neurons: dendritic structure and synaptic integration. Nat. Rev. Neurosci. *9*, 206–221.

Takahashi, N., Kitamura, K., Matsuo, N., Mayford, M., Kano, M., Matsuki, N., and Ikegaya, Y. (2012). Locally synchronized synaptic inputs. Science *335*, 353–356.

Tamás, G., Lörincz, A., Simon, A., and Szabadics, J. (2003). Identified sources and targets of slow inhibition in the neocortex. Science *299*, 1902–1905.

Tran-Van-Minh, A., Cazé, R.D., Abrahamsson, T., Cathala, L., Gutkin, B.S., and DiGregorio, D.A. (2015). Contribution of sublinear and supralinear dendritic integration to neuronal computations. Front. Cell. Neurosci. *9*, 67.

Turrigiano, G. (2011). Too many cooks? intrinsic and synaptic homeostatic mechanisms in cortical circuit refinement. Annu. Rev. Neurosci. *34*, 89–103.

Turrigiano, G.G. (1999). Homeostatic plasticity in neuronal networks: the more things change, the more they stay the same. Trends Neurosci. *22*, 221–227.

Tyagarajan, S.K., and Fritschy, J.M. (2014). Gephyrin: a master regulator of neuronal function? Nat. Rev. Neurosci. *15*, 141–156.

Tyagarajan, S.K., Ghosh, H., Yevenes, G.E., Nikonenko, I., Ebeling, C., Schwerdel, C., Sidler, C., Zeilhofer, H.U., Gerrits, B., Muller, D., et al. (2011). Regulation of GABAergic synapse formation and plasticity by GSK3 -dependent phosphorylation of gephyrin. Proc. Natl. Acad. Sci. *108*, 379–384.

Tyagarajan, S.K., Ghosh, H., Yévenes, G.E., Imanishi, S.Y., Zeilhofer, H.U., Gerrits, B., and Fritschy, J.M. (2013). Extracellular signal-regulated kinase and glycogen synthase kinase 3$\beta$ regulate gephyrin postsynaptic aggregation and GABAergic synaptic function in a calpain-dependent mechanism. J. Biol. Chem. *288*, 9634–9647.

Udakis, M., Pedrosa, V., Chamberlain, S.E.L., Clopath, C., and Mellor, J.R. (2020). Interneuron-specific plasticity at parvalbumin and somatostatin inhibitory synapses onto CA1 pyramidal neurons shapes hippocampal output. Nat. Commun. *11*, 4395.

Villa, K.L., Berry, K.P., Subramanian, J., Cha, J.W., Oh, W.C., Kwon, H.B., Kubota, Y., So, P.T.C., and Nedivi, E. (2016). Inhibitory synapses are repeatedly assembled and removed at persistent sites in vivo. Neuron *89*, 756–769.

Vlachos, A., Reddy-Alla, S., Papadopoulos, T., Deller, T., and Betz, H. (2013). Homeostatic regulation of gephyrin scaffolds and synaptic strength at mature hippocampal GABAergic postsynapses. Cereb. Cortex *23*, 2700–2711.

Wilson, D.E., Whitney, D.E., Scholl, B., and Fitzpatrick, D. (2016). Orientation selectivity and the functional clustering of synaptic inputs in primary visual cortex. Nat. Neurosci. *19*, 1003–1009.

Xu, N., Harnett, M.T., Williams, S.R., Huber, D., O'Connor, D.H., Svoboda, K., and Magee, J.C. (2012). Nonlinear dendritic integration of sensory and motor input during an active sensing task. Nature *492*, 247–251.

Xue, J.-G., Masuoka, T., Gong, X.-D., Chen, K.-S., Yanagawa, Y., Law, S.K.A., and Konishi, S. (2011). NMDA receptor activation enhances inhibitory GABAergic transmission onto hippocampal pyramidal neurons via presynaptic and postsynaptic mechanisms. J. Neurophysiol. *105*, 2897–2906.

Xue, M., Atallah, B.V., and Scanziani, M. (2014). Equalizing excitation-inhibition ratios across visual cortical neurons. Nature *511*, 596–600.

Yasuda, H., Kinoshita, S., and Tsumoto, T. (1998). Localized contribution of N-methyl-D-aspartate receptors to synaptic input-induced rise of calcium in apical dendrites of layer II/III neurons in rat visual cortex. Neuroscience *85*, 1011–1024.

Yuste, R. (2013). Electrical compartmentalization in dendritic spines. Annu. Rev. Neurosci. *36*, 429–449.

Zeng, H., Chattarji, S., Barbarosie, M., Rondi-Reig, L., Philpot, B.D., Miyakawa, T., Bear, M.F., and Tonegawa, S. (2001). Forebrain-specific calcineurin knockout selectively impairs bidirectional synaptic plasticity and working/episodic-like memory. Cell *107*, 617–629.

Zhang, Y., Cudmore, R.H., Lin, D.T., Linden, D.J., and Huganir, R.L. (2015). Visualization of NMDA receptor - dependent AMPA receptor synaptic plasticity in vivo. Nat. Neurosci. *18*, 402–409.

Zita, M.M., Marchionni, I., Bottos, E., Righi, M., Del Sal, G., Cherubini, E., and Zacchi, P. (2007). Post-phosphorylation prolyl isomerisation of gephyrin represents a mechanism to modulate glycine receptors function. EMBO J. *26*, 1761–1771.

## STAR★METHODS

### KEY RESOURCES TABLE

| REAGENT or RESOURCE | SOURCE | IDENTIFIER |
|---|---|---|
| Antibodies | | |
| Anti-vGAT-Oyster 550 | Synaptic System | 131103C3, RRID:AB_887867 |
| Rat monoclonal anti-HA | Roche | 1186742300, RRID:AB_10094468 |
| Qdot® 655 F(ab')2-Goat anti-Rat IgG (H + L) | Thermo Fisher | Q-11621MP, RRID:AB_2556477 |
| Bacterial and virus strains | | |
| AAV1/2-hSyn-Teal-gephyrin-WPRE | This paper | N/A |
| Chemicals, peptides, and recombinant proteins | | |
| BAPTA | Sigma | 85233-19-8 |
| L-NAME | Sigma | N5751 |
| Nifedipine | Sigma | N-7634 |
| Bicuculline | Sigma | 14343 |
| MDL28170 | Sigma | M-6690 |
| KN-93 | Millipore Merck | 422708 |
| KN-92 | Millipore Merck | 422709 |
| APV | Tocris | 0105/50 |
| CNQX | Tocris | 1045/10 |
| ω-conotoxin MVIIC | Tocris | 1084/100U |
| ω-conotoxin GVIA | Tocris | 1085/250U |
| DPNI-caged-GABA | Tocris | 2991/10 |
| MNI-caged-L-glutamate | Tocris | 1490/10 |
| Rhod-2 tripotassium salt | AAT Bioquest | 21067 |
| Alexa Fluor 647 Hydrazide | Thermo Fisher | A20502 |
| Fast Green FCF | Sigma-Aldrich | F7252 |
| Critical commercial assays | | |
| Effectene Transfection Reagent | Qiagen | 301427 |
| Experimental models: Organisms/strains | | |
| Ai9 (B6.Cg-*Gt(ROSA)26Sortm9 (CAGtdTomato) Hze*/J | Jackson Laboratory, USA | JAX:007909, RRID:IMSR_JAX:007909 |
| PVCRE (B6; 129P2-Pvalbtm1(cre) Arbr/J | Jackson Laboratory, USA | JAX:017320, RRID:IMSR_JAX:017320 |
| Parvalbumin-tdTomato (PV-tdTomato) | This paper | N/A |
| Recombinant DNA | | |
| pEGFP-N1 | Clontech | Cat# 632162 |
| pcDNA3 Homer1c::DsRed | Petrini et al., 2009 | N/A |
| pcDNA3 Homer1c::GFP | Petrini et al., 2009 | N/A |
| FingR-Gephyrin-GFP | Gross et al., 2013 | N/A |
| EGFP-Gephyrin | Zita et al., 2007 | N/A |
| Hemagglutinin (HA)-tagged α1 GABAA receptor | Petrini et al., 2011 | N/A |
| pAAV1/2-hSyn-Teal-gephyrin-WPRE | This paper | N/A |
| Software and algorithms | | |
| Metamorph 7.8 | Molecular Devices | http://www.moleculardevices.com/Products/Software/Meta-Imaging-Series/MetaMorph.html RRID: SCR_002368 |
| Clampex 10.6 | Molecular Devices | http://www.moleculardevices.com/products/software/pclamp.html RRID:SCR_011323 |

(*Continued on next page*)

*Continued*

| REAGENT or RESOURCE | SOURCE | IDENTIFIER |
|---|---|---|
| Clampfit 10.7 | Molecular Devices | http://www.moleculardevices.com/products/software/pclamp.html RRID:SCR_011323 |
| MATLAB | Mathworks | http://www.mathworks.com/products/matlab/RRID:SCR_001622 |
| GraphPad Prism 6 | GraphPad | http://www.graphpad.com/ RRID: SCR_002798 |
| Custom program written for MATLAB to reconnect QD trajectories | Petrini et al., 2014; from D Choquet and L Cognet | N/A |
| Custom program for SPT quantifications | Petrini et al., 2014; from D Choquet and A Serge | N/A |
| Leica Application Suite X | Leica Microsystems | https://www.leica-microsystems.com/products/microscope-software/p/leica-las-x-ls/ |

## RESOURCE AVAILABILITY

### Lead contact

Further information and requests for resources and reagents should be directed to and will be fulfilled by the Lead Contact, Andrea Barberis (andrea.barberis@iit.it).

### Materials availability

All unique/stable reagents generated in this study are available from the lead contact with a completed materials transfer agreement.

### Data and code availability

- Microscopy, electrophysiology and SPT data will be shared by the lead contact upon request.
- This paper does not report original code
- Any additional information required to reanalyze the data reported in this paper is available from the lead contact upon request

## EXPERIMENTAL MODEL AND SUBJECT DETAILS

### Animals

All the experiments were carried out in accordance with the laws of Italian Ministry of Health and the guidelines established by the European Communities Council (Directive 2010/63/EU, 2010). Parvalbumin-tdTomato (PV-tdTomato) mice were obtained at the IIT animal facility by breeding Ai9 mice with PVCRE mice. Ai9 (B6.Cg-*Gt(ROSA)26Sortm9(CAGtdTomato) Hze*/J - Jackson Laboratory, USA) mice carrying a *loxP*-flanked STOP cassette, that prevents the transcription of a CAG promoter-driven red fluorescent protein variant (tdTomato) were used as a Cre reporter strain. PVCRE (B6; 129P2-Pvalbtm1(cre)Arbr/J - Jackson Laboratory, USA) mice express the Cre recombinase in Parvalbumin-expressing interneurons without disrupting the endogenous Parvalbumin locus (Pvalb) expression. The resulting offspring PV-td tomato has the STOP cassette removed in Parvalbumin-potitive interneurons and the consequent expression of tdTomato. Mice of either sex were used at P1-P3 for preparing primary neuronal cultures and at P21-P28 to obtain acute slices.

### Primary neuronal cultures

Cultures of hippocampal neurons were prepared from P1-P3 Parvalbumin-tdTomato mice of either sex using a previously published protocol (de Luca et al., 2017) modified from (Baudouin et al., 2012). Briefly, hippocampi were dissected, quickly sliced and digested with trypsin in the presence of DNAase, mechanically triturated, centrifuged at 80g and re-suspended. Neurons were plated at a density of $90 \times 10^3$ cells/mL on poly-D-lysine (0.1 μg/mL) pre-coated coverslips. Cultures were kept in serum-free Neurobasal-A medium (Invitrogen, Italy) supplemented with Glutamax (Invitrogen, Italy) 1%, B-27 (Invitrogen, Italy) 2% and Gentamycin 5 μg/mL at 37°C in 5% CO2 up to 30 days *in vitro* (DIV). During this period, half of the medium was changed weekly. Experiments were conducted at DIV 15-27.

### Acute slices preparation

Horizontal hippocampal slices (300 μm thick) were prepared from P21-P28 mice of either sex, anesthetized using isoflurane and sacrificed by decapitation. Brains were extracted and submerged in ice-cold cutting solution containing: 26 mM NaHCO3, 2 mM

KCl, 1.3 mM NaH2PO4, 20 mM glucose, 200 mM sucrose, 0.4 mM CaCl2, and 8 mM MgCl2 (equilibrated with 95% O2 and 5% CO2). Slices were cut from either hemisphere in ice-cold cutting solution using a vibratome (VT1000S, Leica Microsystems), incubated in a maintenance chamber at ~35°C for 20-30 min in the cutting solution, and subsequently stored at room temperature in artificial cerebrospinal fluid (ACSF). The ACSF solution contained: 125 mM NaCl, 25 mM NaHCO3, 2.5 mM KCl, 1.25 mM NaH2PO4, glucose 25 mM, 2 mM CaCl2, and 1 mM MgCl2, equilibrated at 95% O2 and 5% CO2 for at least 40 minutes.

## METHOD DETAILS

### Plasmid constructs

Enhanced GFP (eGFP) was expressed from the pEGFP-N1 (Clontech). Homer1c-DsRed and Homer1c-GFP plasmids encoding for Homer1c fused with DsRed and GFP at the N terminus, respectively were kindly provided by Dr. D. Choquet (Petrini et al., 2009). EGFP-gephyrin was used previously (Pennacchietti et al., 2017). FingR-gephyrin-GFP (received from Dr C. Duarte) was expressed from pCAG_GPHN.FingR-eGFP-CCR5TC, a plasmid encoding for FingRs (Fibronectin intrabodies generated with mRNA display), that bind endogenous gephyrin with high affinity and allow the visualization of gephyrin clusters using GFP as a reporter (Gross et al., 2013). GABAA receptor α1 subunit carrying the Hemagglutinin (HA) tag between the IV and V amino acid of the mature protein has been described previously (de Luca et al., 2017). The pAAV1/2-hSyn-Teal-gephyrin-WPRE plasmid has been generated by subcloning the DNA sequence encoding the Teal-gephyrin fusion protein from the FU-dio Teal-gephyrin–W plasmid (Addgene #73918) into the AAV-hSyn-IRES-EGFP between NheI e EcoRV sites, thus eliminating both IRES and GFP. The construct was verified by DNA sequencing.

### Transfection and synapse visualization

Neurons were transfected with either using Effectene (*Qiagen*, Germany) at 6-7 days *in vitro* (DIV) or Lipofectamine 2000 (Thermofisher) 24/72 hours before the experiments, following the companies' protocols. All experiments were performed from 14 DIV to 21 DIV. In most experiments, excitatory and inhibitory synapses were visualized by transfecting Homer1c-DsRed and gephyrin-EGFP, respectively. GABAergic synapses were also identified by live immunolabelling of the presynaptic marker vGAT using the anti-vGAT-Oyster550 antibody (Synaptic Systems, Germany) which is directed against the luminal part of the protein, diluted in culture medium and incubated for 30 min at 37°C.

### Viral preparation

Recombinant Adeno-Associated Virus, Serotypes 1,2 (rAAV1/2) expressing the fusion protein Teal-Gephyrin (AAV1/2-hSyn-Teal-Gephyrin-WPRE) used in this study were produced as described previously (McClure et al., 2011). Briefly, adherent HEK293T cells grown in 15 cm plates were transfected by Calcium-Phosphate means with four plasmids containing the adenovirus helper proteins, the AAV Rep and Cap genes 1 and 2, and the ITR-flanked transgene expression cassette. Three days after transfection, cells were harvested, lysed by two freezing-thawing cycles, and treated with benzonase (Merck-Millipore). Viral particles were then purified using heparin columns (Ge HealthCare Life Science). Full capsids were collected. The final product was formulated in sterile phosphate buffered saline and stored at −80°C. Titers of the AAV vector stocks were determined by direct qPCR amplification.

### Viral injection

Bilateral intracerebroventricular injections of AAV1/2-hSyn-Teal-Gephyrin-WPRE were performed on pups of either sex at postnatal day 1. Pups were cryoanesthetized for five minutes before injecting 3 μL of AAV and 0.15 μL of the tracer Fast Green FCF (Sigma-Aldrich) in each hemisphere with a Hamilton syringe equipped with a 33 ga needle. The tracer was used to visualize the injection in the ventriculum. The site of injection was just posterior to bregma, 2 mm lateral to the midline at 3 mm depth. During a following recovery period, pups were placed in a box under a heat lamp for at least 15 minutes before being relocated in their cages and kept with the mother until weaned.

### Antibodies and drugs

Anti-vGAT-Oyster 550 antibody was purchased from Synaptic System (Goettingen, Germany). Anti-HA antibody was from Roche (Milan, Italy). BAPTA (1,2-bis(o-aminophenoxy)ethane-N,N,N′,N′-tetraacetic acid), L-NAME (L-NG-Nitroarginine methyl ester), Nifedipine (1,4-Dihydro-2,6-dimethyl-4-(2-nitrophenyl)-3,5-pyridinedicarboxylic acid dimethylester), and Bicuculline were purchased from Sigma (Milan, Italy). KN-93 and KN-92 were acquired from Millipore Merck (Darmstadt, Germany). APV (D-(−)-2-Amino-5-phosphonopentanoic acid), CNQX (6-Cyano-7-nitroquinoxaline-2,3-dione), ω-conotoxin MVIIC, ω-conotoxin GVIA, DPNI-caged-GABA (1-(4-Aminobutanoyl)-4-[1,3-bis(dihydroxyphosphoryloxy)propan-2-yloxy]-7-nitroindoline) and MNI-caged-L-glutamate ((S)-α-amino-2,3-dihydro-4-methoxy-7-nitro-δ-oxo-1H-indole-1-pentanoic acid) were purchased from Tocris (Bristol, UK). Rhod-2 tripotassium salt was purchased from AAT Bioquest (Sunnyvale, CA, USA).

### Electrophysiological recordings in primary neuronal cultures

Inhibitory and excitatory postsynaptic currents (IPSCs and EPSCs, respectively) were recorded at room temperature in the whole-cell configuration of the patch-clamp technique using the 700B Axopatch amplifier (Molecular Devices, Sunnyvale, CA) and a Nikon

Eclipse Ti microscope. External recording solution contained (in mM): 145 NaCl, 2 KCl, 2 $CaCl_2$, 2 $MgCl_2$, 10 glucose, and 10 HEPES, pH 7.4. Patch pipettes, pulled from borosilicate glass capillaries (Warner Instruments, LLC, Hamden, USA) had a 4 to 5 MΩ resistance when filled with intracellular solution. In all experiments with the exception of paired-patch electrophysiological recordings, the intracellular solution contained (in mM): 10 KGluconate, 125 KCl, 1 EGTA, 10 HEPES, 5 Sucrose, 4 MgATP (300mOsm and pH 7.2 with KOH). Paired-patch recordings were performed with an intracellular solution containing (in mM): 130 KGluconate, 20 KCl, 1 EGTA, 10 HEPES, 5 Sucrose, 4 MgATP (300mOsm and pH 7.2 with KOH). In a subset of paired-patch recordings 20 KCl was replaced with 5 KCl. Since the use of these two intracellular solutions gave comparable results, data were merged. In the paired-patch experiments using BAPTA, 1mM EGTA was replaced with 11mM BAPTA in the presence of 120 mM KGluconate. Currents were recorded using Clampex 10.6 software (Molecular Devices, Sunnyvale, CA). The stability of the patch was checked by monitoring the input resistance during the experiments to exclude cells exhibiting more than 15% changes from the analysis. Currents were sampled at 20 KHz and digitally filtered at 3 KHz using the 700B Axopatch amplifier (Molecular Devices, Sunnyvale, CA). IPSCs and EPSCs were analyzed with Clampfit 10.0 (Molecular Devices, Sunnyvale, CA).

Paired-patch experiments performed with the same electrophysiology rig. A small current was injected into presynaptic neurons in the current clamp mode to keep their membrane potential close to −65 mV. Action potentials, evoked in the presynaptic neuron by injecting depolarizing current pulses (0.8-1 nA for 5-7 ms) at a frequency of 0.1 Hz, elicited IPSCs or EPSCs that were recorded from the postsynaptic neuron voltage-clamped at −65 mV. When the paired-patch involved a presynaptic PV + interneuron and a putative excitatory hippocampal neuron, GABAergic IPSCs were pharmacologically isolated by the continuous perfusion of CNQX (10 μM) to prevent glutamatergic synaptic transmission. When the presynaptic and postsynaptic neurons were two putative excitatory hippocampal neurons, EPSCs were isolated by the continuous perfusion of Bicuculline (10 μM) to prevent GABAergic transmission. IPSCs or EPSCs were continuously acquired from 5 min before to 30 min after the delivery of the electrical plasticity-inducing protocol (see below). IPSCs and EPSCs data were binned in 1 min intervals and normalized to the mean of the baseline amplitude. Data are expressed as normalized values after/before. In the text, we report stimulation-induced average changes in current amplitude between 25 and 30 min after the protocol and expressed as fold-change of the baseline.

### Electrophysiological recordings in acute hippocampal slices

Electrophysiological experiments in acute hippocampal slices were performed using a 700B Axopatch amplifier (Molecular Devices, Sunnyvale, CA) connected to a confocal Leica SP5 microscope equipped with a Photonics VX55 video camera. The same setup also allowed two-photon MNI-glutamate uncaging to elicit uEPSCs and live confocal imaging of Teal-gephyrin. Dentate gyrus granule cells (GCs) were patched with borosilicate glass capillaries (Warner Instruments, LLC, Hamden, USA) filled with intracellular solution containing: 135 mM K-Gluconate, 5 mM KCl, 2 mM NaCl, 10 Na2P-creatine, 0.1 mM EGTA, 10 mM HEPES, 5 mM Mg-ATP, 0.4 mM Na-GTP. Pipettes filled with the intracellular solution showed a resistance of 3-4.5 MΩ. Experiments were performed at room temperature. During the experiment, slices were placed in the recording chamber and superfused with ACSF (see acute slice preparation). Uncaging currents (see also Neurotransmitter uncaging and Plasticity induction) were recorded before and after the induction of plasticity using Clampex 10.6 software (Molecular Devices, Sunnyvale, CA). The stability of the patch was checked by monitoring the input resistance during the experiments to exclude cells exhibiting more than 15% changes from the analysis. Currents were sampled at 20 KHz and digitally filtered at 3 KHz using the 700B Axopatch amplifier (Molecular Devices, Sunnyvale, CA). The amplitude of uEPSCs was analyzed with Clampfit 10.0 (Molecular Devices, Sunnyvale, CA).

### Neurotransmitter uncaging

Neurotransmitter uncaging allows to exogenously elicit uncaging IPSCs (uIPSCs) or EPSCs (uEPSCs) with single-synapse specificity and to keep constant the trial-to-trial amount of neurotransmitter delivered to the postsynaptic element. Inhibitory and excitatory synapses were identified as described above (synapse visualization). In uncaging experiments in neuronal cultures, GABA and Glutamate were photoreleased from DPNI-GABA and MNI-glutamate after illumination by a 378 nm diode laser (Cube 378, 16 mW, Coherent Italia, Italy). MNI-glutamate (5 mM) or DPNI-GABA (1 mM) were dissolved in extracellular recording solution and locally applied near the synapses through a pulled glass capillary (2-4 μm tip diameter) placed at 10-30 μm in the x axis and at 5-10 μm in the z-axis from the region of interest (ROI), using a pressure-based perfusion system (5/10 psi) (Picospritzer, Parker, USA). Such distance was constant in all the experiments to ensure reasonably uniform caged compound concentration across experiments and minimize concentration drop. The laser beam was focused on the sample by means of an Olympus Apo-plan 100X oil-immersion objective (1.4 NA). A beam expander was placed in the optical path between the laser source and the objective in order to achieve a complete filling of the objective pupil, a conditions that maximizes the focusing capability of the objective, thus minimizing the spot size on the sample. The measured point spread function (PSF) had a lateral dimension of 487 ± 55 nm (FWHM, n = 6). The laser beam was steered in the field of view by using a galvanometric mirrors-based pointing system able to illuminate specific regions of interest outlined around glutamatergic and GABAergic synapses defined by Homer1c-DsRed and EGFP-gephyrin (UGA32, Rapp OptoElectronics, Hamburg, Germany). Synchronization of optical uncaging and electrophysiological recordings was controlled with the UGA32 software interfaced with the Clampex 10.0 software (Molecular Devices, Sunnyvale, CA, USA). Both MNI-glutamate and DPNI-GABA uncaging currents (uEPSCs and uIPSCs, respectively) were elicited by 500-1000 μs laser pulses with a power intensity of 80-100 μW at the exit of the objective. In double-uncaging experiments, the same uncaging settings were applied, with MNI-glutamate and DPNI-GABA loaded in two glass capillaries independently positioned in the ROIs and independently controlled by the

aforementioned pressure-based perfusion system. In SPT experiments, when neurotransmitter uncaging was induced, QD-receptor mobility was never monitored, implying that QD illumination never interfered with compounds' uncaging. The time course of uncaging current amplitude changes upon plasticity induction was probed at 10 min intervals and quantified by normalizing the values to the mean of the amplitude at baseline time points. In the text, we report the values of stimulation-induced average changes in current amplitude at 27 min after the protocol expressed as fold-change of the baseline.

In uncaging experiments in acute slices, MNI-glutamate was locally pressure-applied with Picospritzer (Parker Instrumentation) at 5-10 psi. MNI-glutamate (Tocris) at 5 mM concentration was dissolved in ACSF solution and filtered with 0.22 μm syringe filters (Merck Millipore) before being loaded into a glass pipette. The pipette was positioned ~10-30 μm from the spine identified by Alexa 647 fluorescence. In slice experiments a two-photon laser source (720 nm, Chameleon, Coherent) was used for focal photolysis of glutamate (16-20 mW, 10 ms). The laser illumination for eliciting individual uncaging currents (uEPSCs) was controlled by the software Leica Application Suite X, while the delivery of uncaging train pulses (50 Hz) (for the induction of plasticity) was synchronized with the LFS through the Digidata DAC board controlled by Clampex 10.6 software (Molecular Devices, Sunnyvale, CA, USA).

### Plasticity induction

In neuronal cultures, the non-Hebbian plasticity-inducing protocol consisted of action potential (AP) trains elicited in the postsynaptic neuron at 2 Hz for 40 seconds (low frequency stimulation, LFS) in the current clamp configuration. AP was elicited by the injection of depolarizing current pulses (0.8-1 nA for 5-7 ms) (0.8-1 nA for 5-7 ms). Single spine LTP (for a Hebbian stimulation) was induced by pairing the aforementioned LFS with repetitive MNI- glutamate uncaging at 4 Hz at individual spines for 40 seconds (see Neurotransmitter uncaging). Through the text, this protocol has been referred to also as "LFS + MNI-glutamate uncaging". Experiments aimed at identifying the contribution of i) different calcium sources ii) CaMKII role or iii) nitric oxide (NO) role in inhibitory plasticity were performed in the same conditions described above during the bath application of APV (50 μM), L-NAME (50 μM), KN-93 (5 μM), KN-92 (5 μM), ω-conotoxin MVIIC (2 μM), ω-conotoxin GVIA (3 μM) or Nifedipine (10 μM) as described in the text. In the experiments performed to study the involvement of the calpain, neurons were preincubated with the calpain inhibitor III MDL28170 (50 μM) for 30 minutes before the delivery of the single spine LTP protocol.

In acute hippocampal slices, single-spine LTP was induced in dentate gyrus granule cells (GCs) by pairing LFS action potential trains (2 Hz for 40 s) with repetitive two-photon MNI-glutamate uncaging (720 nm illumination wavelength, 50 Hz, 16-20 mW, 10 ms). GCs were filled with the Alexa Fluor 647 dye (20μM) (Thermo Fisher Scientific) to identify spines. The amplitude of uEPSCs evoked at the spines (see Neurotransmitter uncaging) was measured before and 30 minutes after the induction of the single-spine LTP protocol by using the Clampfit 10.7 software (Molecular Devices, Sunnyvale, CA).

### Live-cell imaging

Hippocampal primary cultures from PV-tdTomato mice were transfected with FingR-gephyrin-GFP or EGFP-gephyrin. Samples were illuminated with a LED light source (Spectra X, Lumencor) through 475/34 nm and 543/22 filters (Semrock, Italy). GFP and tdTomato fluorescence was detected using a 520/35 nm and 593/40 nm filters respectively (Semrock, Italy). Neurons positive for GFP were identified, patched and stimulated with the both the non-Hebbian and Hebbian electrophysiological plasticity-inducing protocol. Neurons positive for both GFP and PV-tdTomato were excluded. Images were acquired with the digital camera Hamamatsu, EM-CCD C9100 mounted on a wide field inverted fluorescence microscope (Nikon Eclipse Ti) equipped with an oil-immersion 60X (1.4 NA) or with the digital camera EM-CCD Photometric QuantEM:512SC mounted on a wide field inverted fluorescence microscope (Olympus IX 70) equipped with an oil immersion 100X objective (1.4 NA), for the imaging of EGFP-gephyrin or FingR-gephyrin-GFP clusters, respectively. Acquisition and quantification of gephyrin clusters fluorescence were performed by using the MetaMorph 7.8 software (Molecular Devices).

Images of FingR-gephyrin-GFP or EGFP-gephyrin clusters fluorescence was acquired before and after (up to 30 minutes) the application of the LFS protocol (non-Hebbian stimulation) or the LFS + MNI-glutamate uncaging protocol at individual spines (Hebbian stimulation). Focal plane was set by the operator and maintained fixed for the duration of the experiment. Gephyrin clusters that changed their focal plane after the delivery of the stimulation, were discarded from the analysis. The same light exposure time was used for the acquisition of all images and was set to avoid signal saturation. After background correction, a user-defined intensity threshold was applied to the maximal projection of each image-stack to create a binary mask for the identification of gephyrin clusters. For the analysis of gephyrin clusters, regions were created around each cluster in the binary mask after 2 pixel enlargement. As such, we aimed at avoiding the possibility of underestimating gephyrin fluorescence over time due to the changes in the cluster size/position after the delivery of the protocol. The fluorescence intensity of gephyrin clusters over time was normalized to that quantified before plasticity induction. Values were corrected for the photobleaching quantified in control experiments in which the stimulation was omitted.

Teal-gephyrin live confocal imaging experiments in acute hippocampal slices were performed using an upright confocal microscope (Leica SP5) equipped with a water-immersion 25X objective (0.95 NA) and a 4X magnifier. Dentate gyrus granule cells transduced with AAV1/2-hSyn-Teal-Geohyrin-WPRE were illuminated with an Argon laser light source at 458 nm and 476 nm excitation wavelength and detected by setting a photomultiplier (PMT) in the range 495-555 nm. Alexa Fluor 647 filled into Teal-gephyrin positive GC was illuminated with a HeNe laser source (633 nm) and detected by activating a second PMT set in the 645-700 nm range. Images of a single confocal plane of Teal-gephyrin and Alexa 647 Fluor were acquired with the same settings (line average 8, 400 Hz)

over time, before and at different time points after the induction of the single-spine LTP protocol. These excitation and acquisition parameters were set to avoid signal saturation and were used for the acquisition of all the images over time. After background correction, a user-defined intensity threshold was applied to each image to create a binary mask for the identification of gephyrin clusters and the creation of regions of interest (ROI). The fluorescence of gephyrin clusters was quantified as Teal-gephyrin fluorescence intensity measured in each ROI after background correction. The fluorescence intensity of gephyrin clusters over time was normalized to that quantified before plasticity induction. Values were corrected for the photobleaching quantified in control experiments in which the stimulation was omitted.

### Calcium imaging

Calcium imaging experiments were performed by using Rhod-2 (Minta et al., 1989). The rationale for the choice of this red shifted rhodamine-based calcium indicator with respect to the more commonly used green-emitting indicators was to maximize the separation between the wavelength of the laser used for neurotransmitter uncaging (378 nm) and the indicator absorption spectrum, thus minimizing the possible photobleach of the indicator. Previous studies have shown that the positive net charge of the Rhod-2 molecule favors intracellular Rhod-2 accumulation in mitochondria (Collins et al., 2001). However, this particular Rhod-2 partitioning between cytosol and mitochondria has been mainly observed with the cell permeant form of Rhod-2 (Rhod-2 AM). In contrast, the cell-impermeant form has been used to record bona fide cytosolic calcium in electrophysiological studies (Kaiser et al., 2004; Yasuda et al., 1998). In our calcium experiments with Rhod-2, we observed that, while it efficiently dialyzed in dendrites, it showed limited diffusion into spines. However, since our goal was to study calcium dynamics in the dendritic shaft, we reasoned that such Rhod-2 feature could contribute to maintain unperturbed the spine calcium dynamics, while recording the dendritic one.

Neurons were loaded with Rhod-2 (80 μM) through the patch pipette for at least 5 minutes after reaching the whole-cell configuration to allow the diffusion of Rhod-2 in proximal dendrites. Rhod-2 fluorescence was acquired with the digital EM-CCD QuantEM:512SC camera (Photometrics) mounted on a wide field inverted fluorescence microscope (Olympus IX 70) equipped with an oil-immersion 100X objective (1.4 NA) and the MetaMorph 7.8 software (Molecular Devices). The LFS paired with MNI-glutamate uncaging was delivered at individual spines (Hebbian stimulation). During this protocol, we recorded calcium dynamics in a dendritic region centered below the photostimulated spine. Concomitantly, calcium dynamics was also recorded in another region on a different dendritic branch of the same neuron (at a similar distance from the soma) centered below a reference, non-photo-stimulated spine. Since the latter region was distant from the potentiated spine, it was receiving only the LFS, so hereafter it will be referred to as "LFS" conditions. The onset of calcium responses recorded in the two regions reached plateau in a few seconds after stimulation. Thus, the stimulation protocol duration was reduced to 10 seconds (instead of the full-length stimulation of 40 seconds) in order to minimize fluorescence photobleaching. Therefore, the total duration of the recording was 16 seconds (i.e., 160 frames acquired at 10 Hz) including 3 seconds before (baseline), 10 seconds during and 3 seconds after (recovery) the stimulation protocol.

For the data analysis, we considered dendritic portions of 14 μm centered below the stimulated or the reference spine - which was typically chosen at approximately 10-30 μm from the soma. Every dendritic portion was sub-divided in 7 regions of interest (ROIs) of 2 μm length. The width of each region was adjusted to the thickness of the dendrite. In each region, changes in the Rhod-2 fluorescence intensities induced by the LFS or LFS + MNI-glutamate uncaging were calculated as $\Delta F/F_0$, where $\Delta F$ is the difference between the average fluorescence intensities at plateau and that before the delivery of the protocol. $F_0$ is the average fluorescence intensity measured before the stimulation. In order to quantify calcium variations induced by the pairing of MNI-glutamate uncaging with respect to LFS alone, the $\Delta F/F_0$ recorded upon LFS + MNI-glutamate uncaging was normalized to that observed upon LFS (i.e., Figures 5D and 5E). When considering the spatial spread of calcium variations induced by the stimulating protocols (Figure 5E), the aforementioned normalization was computed for each ROI.

### Quantum dot labelling and imaging

In the experiments aimed at monitoring the modulation of GABAA receptor lateral mobility during spatially-regulated synaptic plasticity, we combined SPT experiments with electrophysiology and plasticity induction (see sections above). Non-Hebbian or Hebbian stimulation protocols were delivered to neurons expressing the HA-tagged α1 subunit of GABAA receptor along with Homer1c-DsRed and EGFP-gephyrin. The surface labelling of the HA tag with QDs allowed to selectively probe the mobility of GABAARs belonging to the neuron that received the plasticity protocol.

Before the experiment, QDs 655 (Invitrogen) were diluted in PBS and pre-exposed to casein 1X (Vectorlab, Italy) for 15 min to prevent QD non-specific binding. Then, living neurons were incubated with the anti-HA antibody (Roche) 1 μg/mL in the electrophysiology external recording solution for 4 minutes and subsequently with the diluted QDs solution for 3 minutes. The final concentration of QD was 0.1 nM. Control experiments omitting the anti-HA antibody were performed to validate the antibody-specific labelling of HA-tagged GABAARs.

SPT experiments were acquired by live-cell imaging on a wide field inverted fluorescence microscope (Olympus IX 70) equipped with a diode-based illumination device (Lumencor, SpectraX Light Engine, Optoprim, Italy), an EM-CCD camera (QuantEM:512SC, Photometrics, pixel size 16 μm) and an Apo-plan oil-immersion 100X objective 1.4 NA (Olympus). For each neuron, we chose a dendritic portion where we first localized glutamatergic and GABAergic synapses by Homer1c-DsRed and EGFP-gephyrin fluorescence acquired with appropriate excitation and emission filter sets (ex: 543/22, 472/30, em: 593/40, 520/35, respectively) to achieve a 2D map of the relative localization of excitatory and inhibitory synapses. QD fluorescence acquired with specific filters (ex: 435/40 and

em: 655/15 filters, Semrock, Italy) was monitored over time by recording movies of 600 consecutive frames at 20 Hz using the Metamorph 7.8 software (Molecular Devices, USA). Please note that QD imaging was never performed during neurotransmitter uncaging, so the 435 nm light was never shed in the presence of caged compounds. The mobility of GABAAR-QD complexes was probed in the same field of view before and 30 minutes after the induction of synaptic plasticity, either with the LFS or with LFS paired with MNI-glutamate uncaging. During the experiments, neurons were kept at 28°C (TC-324B Warner Instrument Corporation, CT, USA) in an open chamber and continuously superfused with the recording solution at 12 mL/h.

### Single particle tracking

Tracking of QD-labelled GABAAR was performed as previously described (de Luca et al., 2017; Petrini et al., 2009). The spatial coordinates of single QDs were identified in each frame as sets of >4 connected pixels using two-dimensional object wavelet-based localization at sub-diffraction limited resolution (~40 nm) using the MIA software which is based on simulated annealing algorithm. Continuous tracking between blinks was performed with an implemented version of custom software originally written in MATLAB (The Mathworks Inc., Italy) in Dr Choquet's lab, based on a QD maximal allowable displacement (4 pixels) during a maximal allowable duration of the dark period. This stringent reconnection of trajectories across QD blinking combined with the highly diluted QD labelling have been set to avoid erroneous reconnection of neighbouring QDs in the same trajectory and to provide unambiguous observations of individual receptor-QD complex trajectories. When, occasionally, two QDs were too close to be unambiguously identified, they both were discarded from the analysis. Receptor trajectories were defined as synaptic (or extrasynaptic) when their spatial coordinates matched (or not) those of clustered EGFP-gephyrin fluorescence. Although the definition of the synaptic compartments was diffraction limited, the sub-wavelength resolution of the single particle detection (~40 nm) allowed accurate description of receptor mobility within such small regions. For each receptor-QD complex, the instantaneous diffusion coefficient, $D$, was calculated from the linear fits of the $n$ = 1–4 values of the MSD versus time plot, using a custom-made software developed by Dr Choquet (Bordeaux, France). For two-dimensional free diffusion, MSD is represented by the equation: $MSD\ (t)=<r^2>=4Dt$ .

*MSD (t)* was calculated according to the formula:

$$<r^2> = \left[\sum_{i=1}^{N-n}(X_{i+n}-X_i)^2 + (Y_{i+n}-Y_i)^2 \Big/ (N-n)\right]dt$$

Only reconstructed trajectories with >80 frames were retained for the analysis. The diffusion coefficients are presented as median and IQR (i.e. the interquartile range) defined as the interval between 25–75% percentiles. The immobile fraction is defined as the relative duration of the residency of a receptor-QD complex in a given compartment with coefficient <0.0075 $\mu m^2\ s^{-1}$. This threshold represents the local minimum of the bimodal distribution of synaptic $GABA_AR$ diffusion coefficients. To achieve a more complete characterization of GABAA receptor diffusion, we also measured the percentage of time spent by each receptor-QD in a given compartment (synaptic or extrasynaptic). In the case of local iLTD, when GABAAR disperse from inhibitory synapses, leaving few receptor-QD complexes for quantification, we also calculated the percentage of receptor number found at synapses after plasticity induction as compared to before the protocol.

## QUANTIFICATION AND STATISTICAL ANALYSIS

For each experiment quantifications and statistical details (statistical significance and test used) can be found in the main text and figure legends. Data are presented as mean ± SEM (standard error of the mean) or as median ± IQR (inter quartile range). For electrophysiological experiments in the paired-patch configuration as well as for gephyrin live-cell imaging (in neuronal cultures and in acute slices) and intracellular calcium imaging experiments n represents the number of neurons observed. In uncaging experiments, the number of synapses (n) is reported along with the number of neurons considered. For SPT experiments, n indicates the number of receptor trajectories, followed by the number of neurons observed. Each experiment was repeated on neurons obtained from at least three different cultures. All acute slices were obtained from different mice. The sample size used in each experiment was based on previous electrophysiological, live-cell imaging and SPT experiments (de Luca et al., 2017; Petrini et al., 2014). Data and statistical analysis was performed using Prism 5.0 and 6.0 Software (GraphPad Prism, USA). Non–normally distributed datasets were tested by two-tailed non-parametric Mann-Whitney U-test, or in the case of paired data by Wilcoxon matched-pairs signed rank test. Statistical differences in time course data within a group was quantified by one-way ANOVA variance test followed by Tukey's multiple comparison test. When possible, RM ANOVA was used, as indicated. Two-way ANOVA variance test was followed by Bonferroni's multiple comparisons test. Indications of significance correspond to p-values as follows: $p < 0.05$ (*), $p < 0.01$ (**), $p < 0.001$ (***) and non-significant (ns), i.e. $p > 0.05$.

**Cell Reports, Volume *38***

## Supplemental information

# Spatial regulation of coordinated excitatory and inhibitory synaptic plasticity at dendritic synapses

**Tiziana Ravasenga, Massimo Ruben, Vincenzo Regio, Alice Polenghi, Enrica Maria Petrini, and Andrea Barberis**

## SUPPLEMENTARY FIGURES

### Figure S1

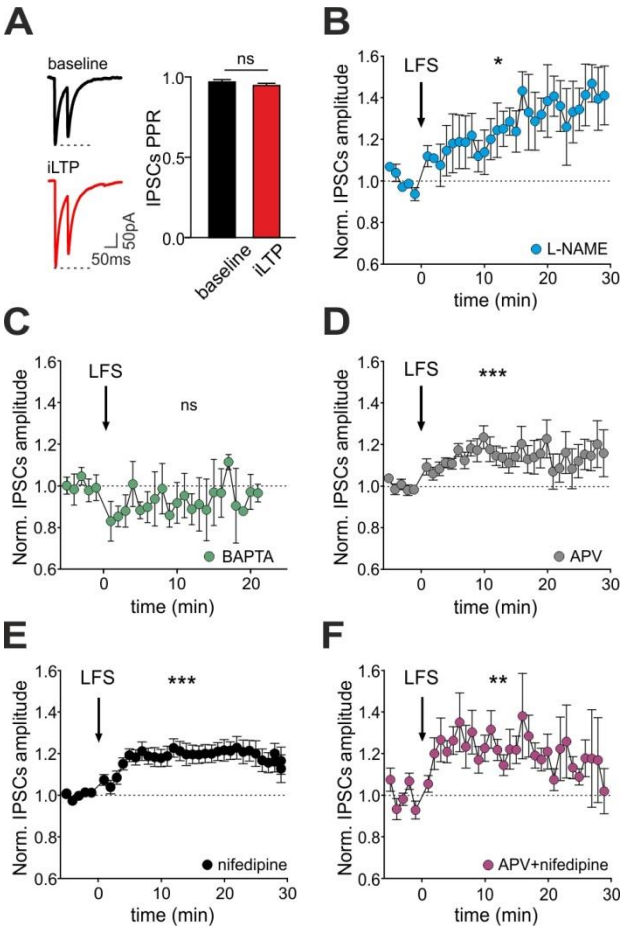


**Figure S1 (related to Figure 1): Postsynaptic mechanism and $Ca^{2+}$ dependence of LFS-induced iLTP**

**A.** Left: Representative IPSC paired pulses traces recorded before (baseline) and after (iLTP) the delivery of the LFS. Right: Quantification of the paired pulse ratio (PPR) (before LFS= 0.96 ± 0.02; after LFS= 0.94 ± 0.02; n = 25; p > 0.05, Wilcoxon matched-pairs test). **B.** The nitric oxide synthase blocker L-NAME does not prevent LFS-induced iLTP (at 25-30 min: normalized IPSCs amplitude = 1.40 ± 0.02 of baseline, n = 5, $F_{33,136}$ = 1.6, p < 0.05; one-way ANOVA followed by Tukey's multiple comparison test). **C-E.** Time course of relative IPSC amplitude changes after the delivery of the LFS protocol (arrow) with respect to baseline, in the presence of the fast $Ca^{2+}$ chelator BAPTA (**C**: 0.97 ± 0.04 fold of baseline, n = 4, $F_{25,69}$ = 0.4, p > 0.05), APV (**D**: 1.16 ± 0.01 fold of baseline, n = 11, $F_{33,241}$ = 2.2, p < 0.001), nifedipine (**E**; 1.16 ± 0.01 fold of baseline, n = 21, $F_{33,640}$ = 3.6, p < 0.001), and APV + nifedipine (**F**: 1.13 ± 0.03 fold of baseline, n = 6, $F_{33,162}$ = 2.1, p < 0.01). One-way ANOVA followed by Tukey's multiple comparison test. Values are expressed as mean ± SEM. *p < 0.05, **p < 0.01, ****p < 0.001, ns = not significant.

**Figure S2**

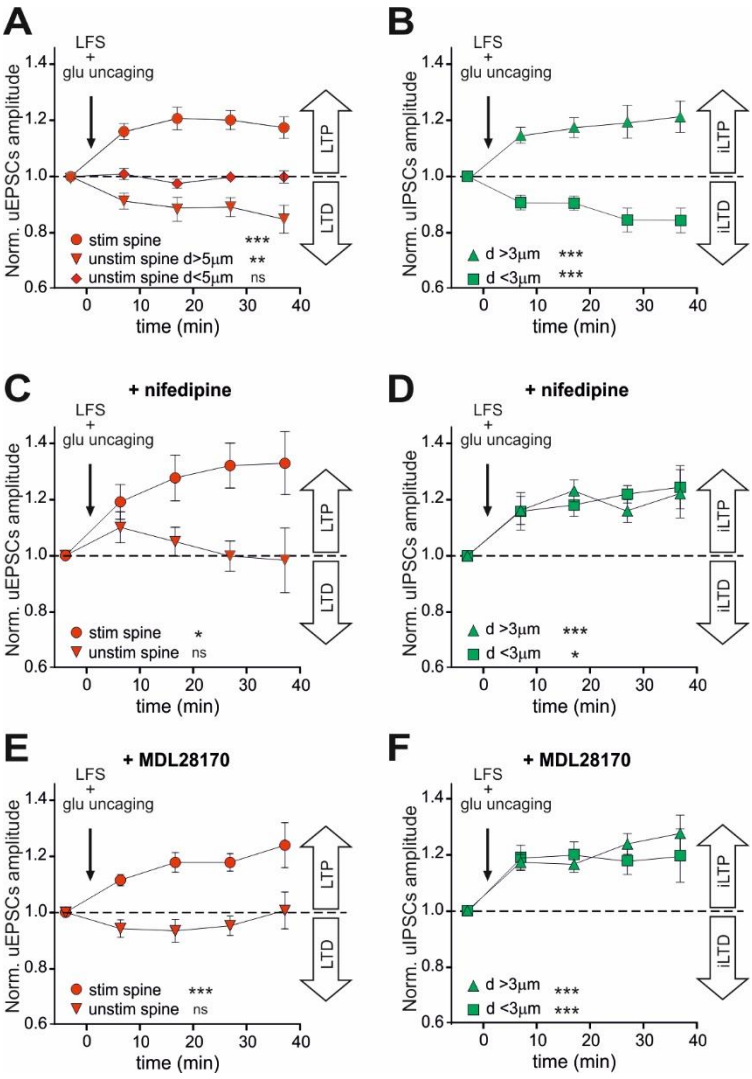


**Figure S2 (related to Figure 4): Spatial coordination of the plasticity of excitatory and inhibitory synapses upon single spine LTP**

**A.** After the single-spine LTP protocol ("LFS+glu uncaging"), the stimulated spine (red circles) is selectively potentiated (each datapoint represents at least n = 9 (max 20) synapses from 22 neurons). Normalized uEPSC amplitude at 27 min = 1.20 ± 0.03 fold, $F_{4,74}$=10.6, p< 0.001). Non-photostimulated spines ("unstim") located more distant than 5µm from the stimulated spine are depressed (red triangles, each datapoint represents at least n = 6 (max 15) synapses from 17 neurons); normalized uEPSC amplitude at 27 min= 0.89 ± 0.03 of baseline, $F_{4,53}$ = 5.4, p < 0.001). Spines located within 5µm from the stimulated spine are not affected by the paired Hebbian protocol (red diamonds, each datapoint represents at least n = 3 (max 5) from 5 neurons); normalized uEPSC amplitude= 0.996 ± 0.002 of baseline, $F_{4,14}$ = 1.2, p > 0.05. **B.** After the "LFS+glu uncaging protocol", GABAergic synapses located at d > 3 µm from the stimulated spine are potentiated (diamond, for each datapoint at least n = 7 (max 42) synapses from 21 neurons); normalized uIPSC

amplitude= 1.20 ± 0.06 of baseline, $F_{4,138}$ = 8.2, p< 0.001. GABAergic synapses located at d < 3 µm from the stimulated spine are depressed (square, at least n = 13 (max 34) synapses from 21 neurons); normalized uIPSC amplitude= 0.85 ± 0.04 of baseline, $F_{4,125}$= 5.7, p < 0.001. **C.** Same as in A in presence of nifedipine. Stimulated spine (red circles): each datapoint represents at least n = 4 (max 7) synapses from 7 neurons. uEPSC amplitude at 27 min: 1.32 ± 0.08 fold increase, $F_{4,26}$ = 3.9, p =0.001. Unstim spine (red triangles): each datapoint represents at least n = 3 (max 6) synapses from 7 neurons. $F_{4,20}$ = 0.8, p > 0.05. **D.** Same as in B, in presence of nifedipine. d < 3 µm (squares): each data point represents at least n = 3 (max 9) synapses from 7 neurons. uEPSC amplitude at 27 min = 1.22 ± 0.03 of baseline, $F_{4,27}$ = 4.0, p < 0.05; d > 3 µm (triangles): each data point represents at least n = 4 (max 13) synapses from 7 neurons; uEPSC amplitude at 27 min = 1.16 ± 0.04 of baseline, $F_{4,45}$ = 6.1, p < 0.001. **E.** Same as in A in presence of MDL28170. Stimulated spine, at least n = 3 (max 23) synapses from 24 neurons, $F_{4,78}$ = 11.9, p < 0.001; unstim spine, at least n = 3 (max 19) synapses from 24 neurons, $F_{4,69}$ = 1.2, p > 0.05. **F.** Same as in B, in presence of MDL28170. d < 3 µm, at least n = 5 (max 20) synapses from 24 neurons, $F_{4,71}$ = 7.1, p < 0.001; d > 3, at least n = 6 (max 43) synapses from 24 neurons, $F_{4,162}$ = 16.7, p < 0.001. Values are expressed as mean ± SEM. All the statistical comparison shown here are performed with one-way ANOVA followed Tukey's post-test. *p < 0.05, ***p < 0.001, ns = not significant.

**Figure S3**

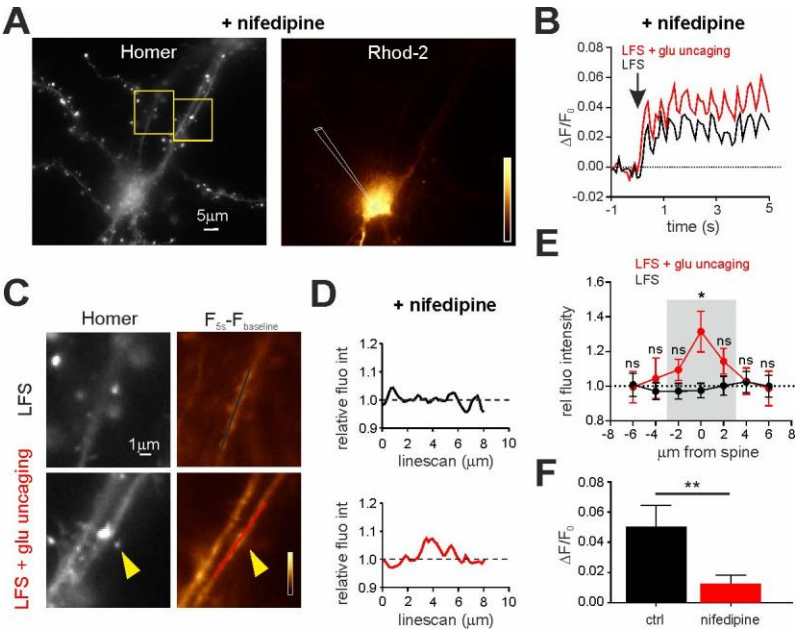


**Figure S3 (related to Figure 5): Spatial dynamics of dendritic calcium in the presence of nifedipine during iLTP and LTD**

**A.** Representative epifluorescence image of a Homer1c-GFP expressing neuron (left) loaded with Rhod-2 through the patch pipette (gold, right). Scale bar, 5 µm. **B.** Relative Rhod-2 fluorescence intensity quantified during the LFS protocol (black) and the LFS paired with glutamate uncaging protocol (red), in the presence of nifedipine. Two 4 µm-long portions of dendrites in the same neuron were considered, one centered below a reference spine and one below the stimulated spine. The arrow indicates the beginning of the protocol. **C.** Left: Magnifications of the dendritic portions framed in A, stimulated with LFS (top) or LFS paired with MNI-glutamate uncaging (bottom). The yellow arrowhead indicates the stimulated spine. Scale bar, 1 µm. Right: Gold pseudocolor representation of Rhod-2 fluorescence intensity changes at plateau (5 s) of the stimulating protocols (i.e., LFS, top and LFS paired with glutamate uncaging, bottom) with respect to baseline values ($F_{5s}$-$F_{baseline}$). The lines indicate the position of the linescans quantified in D. **D**. Relative fluorescence variation induced by "LFS + glu uncaging" protocol with respect to LFS alone, in the presence of nifedipine. The fluorescence intensities quantified along the two linescans in C are normalized to the average fluorescence detected along the linescan in LFS. **E.** Changes in the relative dendritic Rhod-2 fluorescence intensity (as measured in Figure 5D) as a function of the distance from a reference or stimulated spine during the delivery of LFS (black) or the LFS + glu uncaging (red) with nifedipine, respectively. The grey area indicates the range of ± 3µm from the potentiated spine where significant changes in Rhod-2 fluorescence are quantified as compared to the LFS protocol (LFS: n = 13 neurons, LFS+ glu uncaging: n = 13 neurons, $F_{1,168}$ = 5.3, $p < 0.05$, two-way ANOVA followed by Bonferroni's multiple comparison test). Statistical significance for each data point is shown. **F.** Difference of relative fluorescence intensity variation

after the delivery of LFS paired and LFS alone, in the presence of nifedipine (red) or in control (black). Each dendritic region taken in consideration is located within 3 μm from a reference or stimulated spine (control: n = 66, nife: n = 39, $p < 0.01$, Mann Whitney's test). Values are expressed as mean ± SEM. *$p < 0.05$, **$p < 0.01$, ns = not significant, i.e $p > 0.05$.

**Figure S4**

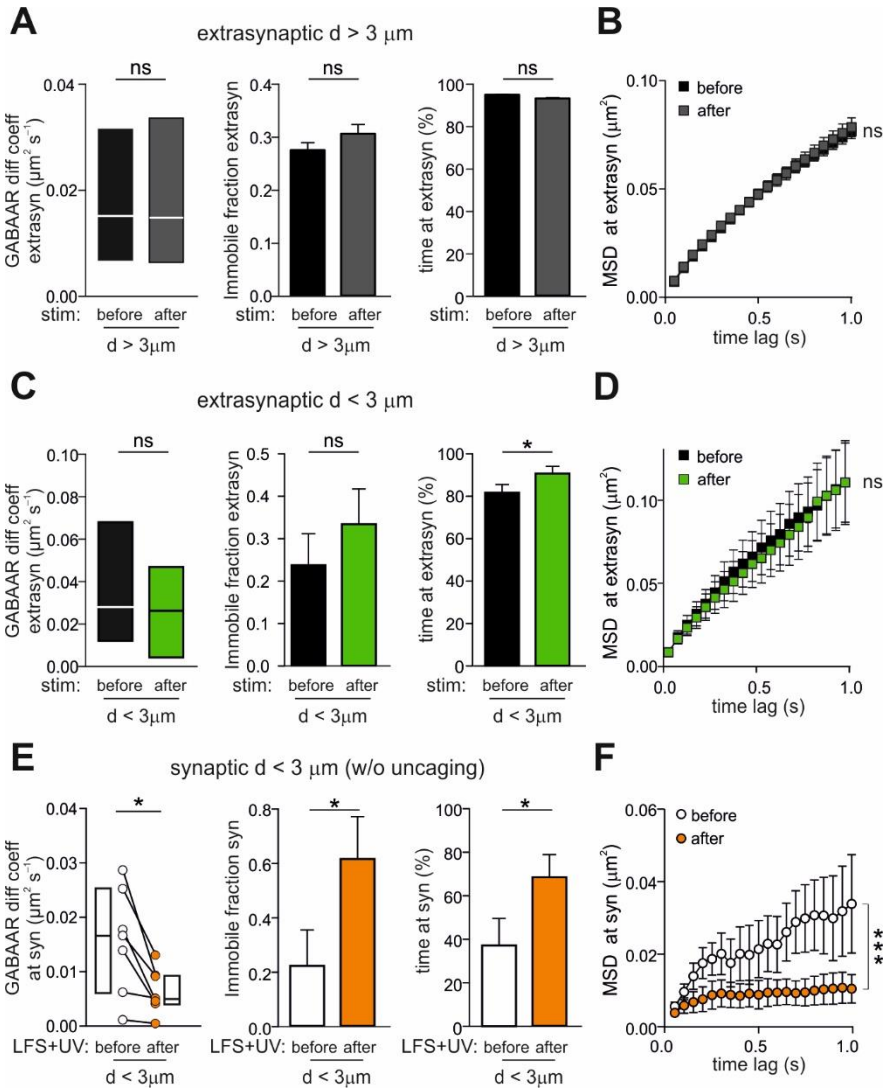


**Figure S4 (related to Figure 7): Supplementary data on the modulation of GABAAR lateral mobility upon single spine LTP**

**A-B.** Characterization of the lateral mobility of extrasynaptic GABAARs located at d > 3 µm from the potentiated spine, before (black) and after (grey) the single spine LTP protocol. **A**. Left: Median diffusion coefficient and interquartile range (IQR) (n = 605-739 trajectories from 28 neurons; $p > 0.05$, Mann-Whitney test). Middle: Immobile fraction (n = 592-795 trajectories from 28 neurons; $p > 0.05$, Mann-Whitney test). Right: Percentage of time spent by GABAA receptors in the extrasynaptic compartment (n = 611-761 trajectories; $p > 0.05$, Mann-Whitney test). **B.** MSD versus time plot (n= 614-845 from 28 neurons; $F_{1,28531} = 0.9$, $p > 0.05$, ordinary two-way ANOVA followed by Bonferroni's post hoc test). **C-D.** Characterization of the lateral mobility of extrasynaptic GABAARs located at d < 3 µm from the stimulated spine, before (black) and after (green) the single spine LTP protocol. **C**. Left: Paired median diffusion coefficient (n = 29

trajectories from 18 neurons; $p > 0.05$, paired Wilcoxon test). Middle: Paired IF (n = 29 trajectories from 18 neurons; $p > 0.05$, paired Wilcoxon test). Right: Paired values of percentage time spent by GABAA receptors in the extrasynaptic compartments at $d < 3$ μm from the stimulated spine (n = 29 trajectories from 18 neurons; $p < 0.05$, paired Wilcoxon test). **D.** MSD versus time plot of paired extrasynaptic GABAA receptors close to the potentiated spine ($d < 3$ μm), (n = 22 from 18 neurons, $F_{1,42} = 0.02$, $p > 0.05$, RM two-way ANOVA followed by Bonferroni's post hoc test). **E-F**. Same as in C-D, except for the uncaging. Please note that in this set of experiments the stimulating protocol was LFS + 4Hz UV-light pulses train on a spine (ctrl spine) in absence of MNI-glutamate. Only synaptic GABAAR trajectories localized in the range of 3μm from the ctrl spine were considered. **E**. Left: Paired median diffusion coefficient (before = 0.017 $\mu m^2 s^{-1}$; IQR: 0.006 – 0.025; after = 0.005 $\mu m^2 s^{-1}$; IQR: 0.004 - 0.09; n = 7 from 4 neurons; $p < 0.05$, paired Wilcoxon test). Middle: Paired IF (before = 0.22 ± 0.13; after = 0.62 ± 0.16; n = 7 from 4 neurons; $p < 0.05$, paired Wilcoxon test). Right: Paired values of percentage of time spent by GABAA receptors at synapses close to the control spine (n = 7 from 4 neurons; $p < 0.05$, paired Wilcoxon test). **F.** Paired MSD values of synaptic GABAA receptors close to the control spine ($d < 3$ μm; n = 4 from 4 neurons, $F_{1,60} = 140$, $p < 0.001$, RM two-way ANOVA). Unless stated otherwise, values are expressed as mean ± SEM. *$p < 0.05$, **$p < 0.01$, ns = not significant.